QUARTERLY JOURNAL OF THE ROYAL METEOROLOGICAL SOCIETY
Q. J. R. Meteorol. Soc. **133**: 1959–1975 (2007)
Published online in Wiley InterScience
(www.interscience.wiley.com) DOI: 10.1002/qj.187

RMetS
ROYAL METEOROLOGICAL SOCIETY

A three-dimensional mountain wave imaged in satellite radiance throughout the stratosphere: Evidence of the effects of directional wind shear

Stephen D. Eckermann,[a]* Jun Ma,[b] Dong L. Wu[c] and Dave Broutman[b]
[a] *Space Science Division, Naval Research Laboratory, Washington DC, USA*
[b] *Computational Physics Inc, Springfield, Virginia, USA*
[c] *Jet Propulsion Laboratory, California Institute of Technology, Pasadena, California, USA*

ABSTRACT: Swath-scanned thermal radiances from the Advanced Microwave Sounding Units (AMSU-A) on the NOAA and Aqua satellites are used to image the horizontal temperature structure of a long-wavelength mountain wave that formed over southern Scandinavia on 14 January 2003. Data from all six stratospheric channels show this wave propagating through the full depth of the stratosphere. In channels 9–11 (altitudes ∼20–90 hPa) the imaged wave has a phase structure broadly consistent with a stationary wave radiated by the southeastward flow over and above the quasi-elliptical terrain of southern Norway. Channel 12 radiances at ∼10 hPa, however, show a remarkable abrupt change in imaged wave structure: the horizontal wavelength contracts, phase lines rotate anticlockwise by 30°–40°, and peak activity migrates to the south to lie over Denmark and northern Germany. Similar structure persists in channels 13 and 14 (at ∼2–5 hPa) with progessively increasing radiance amplitudes. These features are stable over the ∼10 hours of AMSU-A measurements from five separate overpasses, and are validated against independent radiances acquired by the Atmospheric Infrared Sounder (AIRS) and retrieved AIRS/AMSU-A temperature profiles from the Aqua overpass.

This change at the channel 11/12 interface coincides with an onset of anticlockwise rotation (backing) and intensification of background stratospheric winds with height. Fourier-ray and spatial ray modelling incorporating these directionally sheared winds and simplified orographic forcing reproduce the salient features of the observations, but only after wave-induced temperature perturbations have been converted to channel radiances using a forward model. The differential visibility of various components of this three-dimensional mountain wave to the AMSU-A channel weighting functions has a first-order impact on the observations at heights above 10 hPa. Once that is factored in, the combined observations and modelling provide direct experimental support for the Shutts model's predictions of how backing wind vectors affect the vertical evolution of three-dimensional mountain waves. Implications of these observations for orographic gravity wave drag parametrization are briefly discussed. Copyright © 2007 Royal Meteorological Society

KEY WORDS radiance imagery; AMSU-A; AIRS; directional wind shear; asymptotic wake

Received 25 June 2007; Revised 16 October 2007; Accepted 19 October 2007

1. Introduction

Soon after the discovery of an ozone hole over Antarctica, an intensive aircraft campaign to measure ozone and related chemical, dynamical and microphysical processes in the Arctic winter stratosphere was conducted from an operating base in southern Scandinavia (Turco *et al*., 1990). Since then, stratospheric field campaigns based in Scandinavia have been conducted at fairly regular intervals (e.g. Pyle *et al*., 1994; Stefanutti *et al*., 1999; Newman *et al*., 2002; Lowe *et al*., 2006). As a result, the stratosphere in and around Scandinavia has arguably been measured in greater detail than any other stratospheric region on the planet.

The early measurement campaigns reported strong correlations between polar stratospheric clouds (PSCs) and mountain waves forced by flow across the Scandinavian mountains (Deshler *et al*., 1994; Godin *et al*., 1994), which subsequent modelling showed could attain large amplitudes and form PSCs in their cooling (ascent) phases (Volkert and Intes, 1992; Leutbecher and Volkert, 1996). This motivated follow-up campaigns which systematically forecast these waves (Dörnbrack *et al*., 1998; Eckermann *et al*., 2006b), using this guidance to devise quasi-Lagrangian aircraft flights to observe stratospheric microphysics upstream, within and downstream of the forecast waves (e.g. Wirth *et al*., 1999). In addition to revealing how mountain waves can significantly affect solid PSC formation, denitrification and chlorine activation on both a regional and hemispheric scale (e.g. Carslaw *et al*. 1998, 1999; Fueglistaler *et al*., 2003; Kuhl *et al*., 2004; Mann *et al*., 2005; Lowe *et al*., 2006), these measurements, together with their associated

* Correspondence to: Stephen D. Eckermann, Naval Research Laboratory, 4555 Overlook Ave SW, Washington DC 20375, USA.
E-mail: stephen.eckermann@nrl.navy.mil

modelling support, have provided a detailed picture of the long-wavelength stratospheric mountain waves that form over different parts of Scandinavia during winter (e.g. Dörnbrack *et al*., 2001; Hertzog *et al*., 2002; Eckermann *et al*., 2006b).

Detailed suborbital wave measurements like these have proven particularly valuable since, until recently, both global models and satellite remote sensors have lacked the necessary spatial resolution to resolve mountain waves. For example, flow over complex orography can generate a spectrum of mountain waves with horizontal wavelengths between ∼5 and 500 km. Climate models have typical horizontal gridbox resolutions $\Delta L \sim 100$ km and cannot accurately resolve dynamics with scales shorter than $\sim 6\Delta L - 10\Delta L$ (e.g. Davies and Brown, 2001; Skamarock, 2004), while satellite limb-sounding measurements typically have horizontal averaging widths along the line of sight of ∼200 km (e.g. Preusse *et al*., 2002). Consequently the important influences of orographic gravity wave drag on the climate and meteorology of the extratropical winter stratosphere and mesosphere and of mountain waves on PSC formation and ozone loss must be parametrized in global middle atmosphere models (e.g. McLandress, 1998; Pierce *et al*., 2003; Mann *et al*., 2005; Siskind *et al*., 2007). These parametrizations incorporate various simplifying assumptions that are difficult to validate due to the paucity of mountain wave data from satellites.

However, advances in computing power and satellite remote sensing technology have seen the longer-wavelength 'outer scales' of the gravity wave spectrum explicitly resolved by the latest global numerical weather prediction (NWP) models and satellite remote sensors (e.g. Wu and Eckermann, 2007). Since resolved waves exist near the resolution limits of these systems, it is important to study and validate these new global gravity wave signals. Scandinavia is an ideal location for such validation studies, since measurements and modelling have shown that the wide Scandinavian mountain ranges force mountain waves with horizontal wavelengths long enough for high-resolution global models and satellite remote sounders to resolve. The campaigns here also provide suborbital wave measurements that are needed to validate these resolved mountain wave signals independently.

Eckermann *et al*. (2006a) provided a start in this regard. They focused on a long-wavelength stratospheric mountain wave that formed over southern Scandinavia on 14 January 2003 during the second SAGE (Stratospheric Aerosol and Gas Experiment) III Ozone Loss and Validation Experiment (SOLVE II), based in Kiruna, Sweden. This wave was forecast in the field and predicted to form ice PSCs, which prompted a science flight of NASA's instrumented DC-8 research aircraft that underflew the forecast wave and profiled the stratosphere with on-board aerosol and temperature lidars. Eckermann *et al*. (2006a) performed high-resolution simulations of this measurement day using both global and mesoscale NWP models, which revealed a large-amplitude stratospheric mountain wave whose cold phases correlated closely with ice PSCs in the DC-8 aerosol lidar data and temperature minima below the frost point in vertical temperature profiles from the DC-8 lidar and a nearby radiosonde. They then showed that this wave was resolved in radiances from a lower stratospheric (∼90 hPa) thermal channel of the Advanced Microwave Sounding Unit-A (AMSU-A) instruments on the NOAA and Aqua polar-orbiting satellites. Forward modelling of the wave-modulated NWP temperature fields yielded radiance perturbations very similar in amplitude and horizontally imaged phase structure to these AMSU-A observations, validating the gravity wave detection capabilities of this instrument channel derived theoretically by Eckermann and Wu (2006).

Since Scandinavian field campaigns have for the most part focused on lower-stratospheric ozone, they have acquired much less data on mountain wave properties in the upper stratosphere and mesosphere, where mountain wave breaking is believed to exert major influences on the large-scale climate (e.g. McLandress, 1998; Siskind *et al*., 2007), with effects extending into the lower stratosphere through modified diabatic descent rates (e.g. Garcia and Boville, 1994). Such factors motivated the Mountain and Convective Waves Ascending Vertically (MaCWAVE) field campaign in Esrange, Sweden from 24 to 30 January 2003 (Goldberg *et al*., 2006), which overlapped with SOLVE II. Unfortunately, a sudden stratospheric warming severely inhibited the propagation of Scandinavian mountain waves into the mesosphere during MaCWAVE (Blum *et al*., 2006). Conversely, the SOLVE II mountain wave event of 14 January occurred just prior to this warming when the vortex, despite being displaced off the pole, was still relatively stable and strong vortex edge winds were located over southern Scandinavia (McCormack *et al*., 2004). This provided a local environment theoretically conducive to mountain wave propagation throughout the stratosphere.

We investigate this possibility experimentally in this study by extending the satellite analysis of Eckermann *et al*. (2006a) to all six AMSU-A stratospheric thermal channels, which are introduced and modelled for their visibilities to three-dimensional (3D) gravity waves in Section 2. Those data are analyzed for their mountain wave content over Scandinavia on 14 January 2003 in Section 3, revealing wave oscillations in all channels and a remarkable and sudden change in the wave's imaged horizontal phase structure at ∼10–20 hPa that is also seen in independent data from the Aqua satellite overpass. We study the synoptic environment accompanying this event in Section 4, which provides guidance for modelling and interpreting these wave observations in Section 5. In Section 6 we consider this wave's momentum flux, mesospheric impacts and the broader implications for mountain wave drag parametrization in global models. Major findings are summarized in Section 7.

DOI: 10.1002/qj

2. Data and models

2.1. AMSU-A thermal radiances

AMSU-A is a nadir-viewing cross-track scanner whose channel properties and scanning patterns are described in Section 2 of Eckermann and Wu (2006) and references therein. It acquires radiances at $j = 1$–30 off-nadir cross-track viewing angles β_j distributed symmetrically about nadir between $\pm 48.33°$. One scan consists of successive staring measurements of $\sim$0.2 s duration stepped in $\Delta\beta_j$ increments of 3.33°. Here we analyze data acquired by the four AMSU-A instruments that were operating on the NOAA 15–17 meteorological satellites and NASA's Earth Observing System (EOS) Aqua satellite during our period of interest (January 2003). Since all four satellites are polar orbiters, this gives eight AMSU-A overpasses of a given region per day.

We focus on data from the six stratospheric temperature sounding channels $C = 9$–14. Eckermann and Wu (2006) describe a simple forward model for deriving 3D weighting functions for AMSU-A channel 9 at beam positions $j = 1 \ldots 15$, denoted $W_j^{C=9}(X, Y, Z)$, where X is along-track distance, Y is cross-track distance, and Z is pressure height (Figure 1 of Eckermann and Wu, 2006). To extend to channels 9–14, we retain their spherical ray model and parametrizations of scanning/orbital specifics and antenna patterns, but replace their analytical approximation of the channel 9 absorption with numerical output from the Joint Center for Satellite Data Assimilation (JCSDA) Community Radiative Transfer Model (CRTM; Kleespies *et al*. 2004). Our CRTM calculations used reference 1D vertical profiles of temperature and water vapour and ozone mixing ratios for 14 January 2003 over southern Scandinavia taken from analysis fields described in Section 2.3. The version of the CRTM used here did not include Zeeman splitting effects on these oxygen lines, an omission that should only be significant for channel 14 (Rosenkranz 2003).

The resulting weighting functions $W_j^C(X, Y, Z)$ for beams $j = 1$–15 and $C = 9$–14 are profiled in Figure 1. Right panels show the 1D vertical weighting functions

$$w_j^C(Z) = \int \int_{-\infty}^{\infty} W_j^C(X, Y, Z) \mathrm{d}X \mathrm{d}Y, \qquad (1)$$

at the near-nadir ($j = 15$) and far off-nadir ($j = 1$) beam positions, normalized such that

$$\int_0^{\infty} w_j^C(Z) \mathrm{d}Z = 1.$$

Left panels show 2D Y–Z cross-sections through the peak $W_j^C(X, Y, Z)$ responses. Since scanning is symmetric about the subsatellite point ($Y = 0$), such that $\beta_{j_*} = -\beta_j$ where $j_* = 31 - j$, the weighting functions at the $j_* = 16$–30 conjugate beam positions at $Y > 0$ are given by $W_{j_*}^C(X, Y, Z) = W_j^C(X, -Y, Z)$.

The results in Figure 1 reproduce various well-known properties of these weighting functions. First, vertical

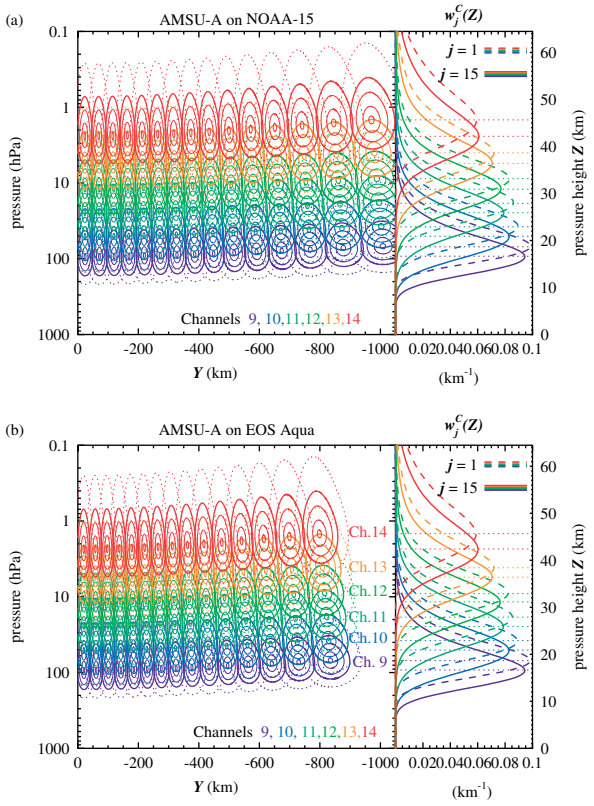

Figure 1. Left panels show 2D cross-sections through peak $W_j^C(X, Y, Z)$ response as a function of pressure height Z and cross-track distance Y, from forward model calculations for AMSU-A channels $C = 9$–14 on the (a) NOAA and (b) Aqua satellites. W_j^C values are normalized relative to the peak response: solid contours show the 0.99, 0.9 and 0.7 levels, the bold solid contour is 0.5, and the dotted contour is 0.2. Right panels show 1D vertical weighting functions $w_j^C(Z)$ for beams nearest ($j = 15$, solid curves) and farthest ($j = 1$, dashed curves) from nadir. This figure is available in colour online at www.interscience.wiley.com/qj

widths increase with increasing channel number C, while horizontal diameters, or 'footprint' widths, increase with increasing $|\beta_j|$. For a given channel C, the altitude of peak response increases with increasing $|\beta_j|$ due to the limb effect. The different cross-track swath widths for Aqua and NOAA are due to different orbit altitudes (705 km for Aqua, 833 km for the NOAA satellites). The nominal peak altitudes of each channel's weighting functions, evident in Figure 1, are summarized in Table I.

Table I. AMSU-A stratospheric channel properties.

Channel number	Nominal altitude (hPa)	Noise floor (NEΔT, K)
14	2.5	0.8
13	5	0.5
12	10	0.35
11	25	0.25
10	50	0.2
9	90	0.15

DOI: 10.1002/qj

We analyze the Level 1b radiances, expressed as brightness temperatures T_B. Radiances were not limb-adjusted (Goldberg *et al.*, 2001) and thus retain the altitude variation versus scan angle due to the limb effect depicted in Figure 1.

Following Eckermann and Wu (2006), the 'visibility' of AMSU-A radiances to a plane monochromatic gravity wave of wavenumber (k_X, k_Y, k_Z) and some given constant peak temperature amplitude is given approximately by

$$V_j^C(k_X, k_Y, k_Z) = \frac{|\widetilde{W}_j^C(k_X, k_Y, k_Z)|}{|\widetilde{W}_j^C(0, 0, 0)|}, \qquad (2)$$

where $\widetilde{W}_j^C(k_X, k_Y, k_Z)$ is the Fourier transform of $W_j^C(X, Y, Z)$. The denominator in (2) normalizes on the assumption that AMSU-A measurements at all beam positions and channels can perfectly measure the brightness temperature of an atmosphere in which temperature does not vary spatially ($V_j^C(0, 0, 0) = 1$).

Figure 2 plots visibility cross-sections $V_j^C(k_X = 0, k_Y, k_Z)$, appropriate for a plane gravity wave propagating along the (Y, Z) plane. Columns show results for channels 9 and 13 at the beam position extrema of $j = 1$ (farthest off-nadir) and $j = 15$ (closest to nadir). Rows show differences between AMSU-A on the NOAA and Aqua satellites. As in Eckermann and Wu (2006), the 0.1 (10%) visibility contour is highlighted as a working lower bound for detectability of a gravity wave in AMSU-A radiances. Actual limits are determined by the wave's brightness temperature amplitude relative to the channel noise floors, which are listed in Table I as noise equivalent delta temperatures (NEΔT: Mo, 1999; Lambrigtsen, 2003; Wu, 2004).

The same general trends in gravity wave visibility discussed in depth by Eckermann and Wu (2006) for channel 9 are noted here for all channels. Visibilities are broadly symmetric with respect to negative and positive scan angles. Visibilities reduce sharply with decreasing vertical wavelength $\lambda_Z = 2\pi/|k_Z|$ for all channels and beam positions, with all waves of $\lambda_Z \lesssim 10$ km essentially invisible to AMSU-A. While horizontal wavelengths $\lambda_Y = 2\pi/|k_Y|$ as short as $\sim$100 km are visible in radiances from near-nadir beams, they are invisible to the off-nadir beams due to broadening of the horizontal measurement footprints.

2.2. AIRS thermal radiances and AIRS/AMSU/HSB temperature retrievals from Aqua

AMSU-A operates synchronously on NOAA satellites with its sister AMSU-B instrument, which acquires radiances from water vapour lines for humidity profiling. Aqua includes an AMSU-B clone with the 89 GHz channel removed, called the Humidity Sounder for Brazil (HSB; Lambrigtsen and Calheiros, 2003). The AMSU on Aqua also operates synchronously with the hyperspectral Atmospheric Infrared Sounder (AIRS), forming the integrated AIRS/AMSU/HSB (AAH) sounding system (Aumann *et al.*, 2003; Chahine *et al.*, 2006). Both HSB and AIRS have horizontal measurement footprints three times smaller than AMSU-A, with scanning synchronized so that 3×3 AIRS and HSB footprints fall within every AMSU-A measurement footprint, known colloquially as the AIRS 'golf ball'.

Here we study version 3.0.8 Level 1b radiances from a small subset of AIRS stratospheric thermal sounding channels. In the upper stratosphere, we analyze radiances

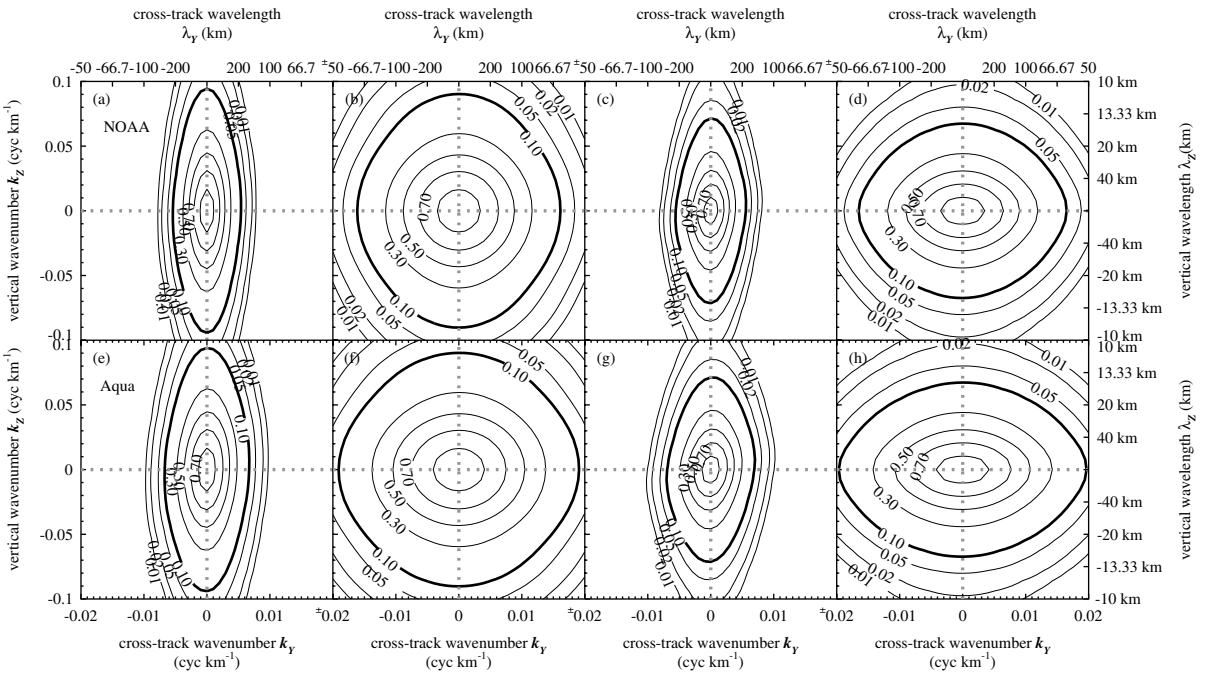

Figure 2. Visibilities $V_j^C(0, k_Y, k_Z)$ for AMSU-A on NOAA satellites for channel 9 at beam positions (a) $j = 1$ ($\beta_j = -48.33°$) and (b) $j = 15$ ($\beta_j = -1.67°$). (c) and (d) show corresponding results for channel 13. (e)–(h) are as (a)–(d), but for the AMSU-A on EOS Aqua.

DOI: 10.1002/qj

from channels 72, 75 and 79, centred at wavenumbers of 667.018, 667.775 and 668.787 cm^{-1} and peaking at altitudes ~30, ~2.5 and ~10 hPa, respectively. In the lower stratosphere, wave-induced infrared radiance signals have smaller amplitudes and are highly susceptible to contamination by tropospheric clouds (Aumann *et al*., 2003; Alexander and Barnet, 2007). The ice PSCs produced by the wave in our case-study (Figure 11 of Eckermann *et al*., 2006a) may also contaminate AIRS radiances (Stajner *et al*., 2007). Thus, to improve signal to noise, here we synthesized a fourth AIRS radiance product by averaging Level 1b radiances from 14 independent AIRS channels that peak at or near 80 hPa: specifically, channels 92, 98, 104, 105, 110, 111, 116, 117, 122, 123, 128, 129, 134, and 140.

More effective removal of cloud effects from AIRS thermal radiances occurs during the AAH temperature retrieval, where the coregistration of AMSU-A, AIRS and HSB measurements on Aqua is used to perform 'cloud clearing' of the AIRS radiances (Susskind *et al*., 2003, 2006). This is achieved at the expense of desampling the cloud-cleared AIRS radiances, and hence the retrieved AAH temperature profiles (hereafter denoted T_A), to the coarser AMSU-A horizontal footprint resolution. The pay-off, however, is retrieved temperature profiles $T_A(Z)$ with a vertical resolution ΔZ far exceeding both the AMSU-A and AIRS radiances, due to input from scores of additional AIRS thermal and water vapour channels (Section 2.2 of Susskind *et al*., 2006). Tests against meteorological analysis fields indicate that stratospheric T_A profiles are accurate to at least ~ 1–2 K with $\Delta Z \sim$ 3 km, with tropospheric profiles near the 1 K/1 km AAH science goal (Susskind *et al*., 2006).

Here we analyze T_A profiles from the version 4.0.21 AAH retrievals with HSB radiances included, since our period of interest occurred just prior to the failure of the Aqua HSB. We use the high-vertical-resolution 'support' product issued at $k = 1 \ldots 100$ (oversampled) pressure levels p_k from $\sim$ 1000–0.1 hPa.

2.3. Analysis fields

To study the large-scale meteorology associated with the gravity wave signals in the satellite radiances and temperature retrievals, we use global atmospheric analysis fields from:

- a Navy Operational Global Atmospheric Prediction System (NOGAPS) reanalysis using the Naval Research Laboratory (NRL) Atmospheric Variational Data Assimilation System (NAVDAS), as described by Eckermann *et al*. (2006a). These fields are issued on a $1^\circ \times 1^\circ$ grid at reference pressure levels from the ground to 4 hPa.
- NASA's Global Modeling and Assimilation Office (GMAO) version 4 Global Earth Observing System's (GEOS-4) 'late look' analyses, issued on a $1.25^\circ \times 1^\circ$ grid on standard pressure levels from the ground to 0.2 hPa (Bloom *et al*., 2005).

For the spatial ray-tracing experiments described in Section 2.4, we combined the NAVDAS analyses from 1000 to 10 hPa with GMAO analyses from 10 to 0.4 hPa to provide a hybrid high-altitude 1000–0.4 hPa analysis product through which to trace gravity waves. Geopotential heights were combined by successively adding the GMAO thickness increments at pressure altitudes above 10 hPa to the 10 hPa NAVDAS geopotential heights.

We also use analyzed mean-sea-level pressure (MSLP) from the $2.5^\circ \times 2.5^\circ$ reanalyses issued by the National Centers for Environmental Prediction (NCEP) and the National Center for Atmospheric Research (NCAR).

2.4. Ray models

We use two ray-based gravity-wave models to help interpret apparent mountain wave signals in the AMSU-A radiances and AAH temperature retrievals.

2.4.1. GROGRAT

We perform 3D spatial ray tracing using the Gravity Wave Regional or Global Ray Tracer (GROGRAT; Marks and Eckermann, 1995; Eckermann and Marks, 1997). The model configuration used here reads in a regional cube of horizontal winds, temperatures and geopotential heights on reference pressure levels, interpolates them onto a regular geometric height grid and fits cubic splines in all three spatial dimensions to allow these fields and all their spatial derivatives to be evaluated at any point within the domain. Ray solutions are computed by numerically integrating the spatial ray equations of Marks and Eckermann (1995) within this domain using a fourth-order Runge–Kutta method.

In the experiments reported here, ray path modifications due to time variations in the background atmosphere are not considered. Wave amplitudes are computed along ray paths using a 1D form of the wave action continuity relation that conserves the vertical flux of wave action density spatially, in the absence of dissipation. Wave amplitudes are dissipated through wave breaking due to convective and dynamical instabilities (Fritts and Rastogi, 1985), vertical scale-dependent infrared radiative damping (Zhu, 1993), and climatological background vertical diffusivities. (Marks and Eckermann (1995) and Eckermann and Marks (1997) provide further details.)

2.4.2. Fourier-ray model

We also compute linear mountain wave solutions for purely vertical environmental profiles using the Fourier-ray algorithm described by Broutman *et al*. (2003).

The form of the model used here computes steady-state ($t \to \infty$) vertical displacement solutions η for linear stationary gravity waves forced by flow over arbitrary surface topographic elevations $h(x, y)$ and vertical profiles of the background wind vector $\mathbf{U}(z)$, Brunt–Väisälä frequency $N(z)$ and density $\rho(z)$. The algorithm derives ray solutions $\eta(k, l, z)$ for both trapped and free propagating modes (Broutman *et al*., 2003), where (k, l) is

DOI: 10.1002/qj

the horizontal wavenumber, using a non-hydrostatic compressible dispersion relation. Spatial wave field solutions $\eta(x, y, z)$ follow from the 2D inverse horizontal Fourier transform of the ray solutions $\eta(k, l, z)$ at any given z.

Since no physical dissipation processes (e.g. parametrized wave breaking) are applied here, wave-induced temperature perturbations follow from the standard adiabatic relation (e.g. Eckermann *et al*., 1998)

$$T'(x, y, z) = -\left[\frac{\overline{T}(z)N^2(z)}{g}\right]\eta(x, y, z), \qquad (3)$$

where $\overline{T}(z)$ is the background temperature profile and g is gravitational acceleration.

To reduce the potential for horizontal wraparound, the model was run here in a broad $3072 \times 3072 \times 59$ point domain with $\Delta x = \Delta y = 2$ km and $\Delta z = 1$ km, with results shown only in the central 1000×1000 points of the domain. Additionally, following Broutman *et al*. (2003), we impose a small imaginary horizontal wavenumber component of 1.3×10^{-8} m^{-1}, which significantly damps only those trapped resonant modes that propagate long distances downstream of the mountain, further minimizing the potential for wraparound.

3. Mountain wave imagery

3.1. AMSU-A radiances

From the raw swath-scanned brightness temperatures T_B in each channel, we isolate gravity wave radiance perturbations T'_B by fitting and removing the large-scale background radiance $\overline{T}_B$ using the algorithm described in Section 5.1 of Eckermann *et al*. (2006a). To reduce noise, a 3×3 point running average was applied in the along- and cross-scan directions, yielding effective noise floors for these maps that are a factor of 3 smaller than those listed for single measurements in Table I.

Figure 3 presents a time–height montage of imaged AMSU-A brightness temperature perturbations $T'^C_B(\widehat{\lambda}_{ij}, \widehat{\phi}_{ij})$ on 14 January 2003 for channels $C = 9$–14, where $(\widehat{\lambda}_{ij}, \widehat{\phi}_{ij})$ is the centroid footprint longitude and latitude for scan i and beam position j. Imagery is arranged with channel altitude increasing vertically and overpasses in chronological order from left to right.

The channel 9 data in the bottom row of Figure 3 have been analyzed and modelled previously by Eckermann *et al*. (2006a). They performed high-resolution meteorological and forward radiance modelling to show that these perturbations were produced by a mountain wave with a peak temperature amplitude T_{peak} ~6–7 K, vertical wavelength $\lambda_Z \sim 12$ km and horizontal wavelength $\lambda_h \sim 400$ km.

The channel 10–11 T'_B imagery in Figure 3 shows a very similar horizontal mountain wave structure, though changed in phase, consistent with the $\lambda_Z \sim 12$ km inferred by Eckermann *et al*. (2006a). Channel 10 radiances reveal weaker T'_B amplitudes than for channel 9, consistent with weaker 50 hPa wave amplitude in the simulations of Eckermann *et al*. (2006a, their Figure 8) and slightly broader vertical weighting functions (smaller visibilities) for channel 10 relative to channel 9 (Figure 1). Channel 11 radiances, which peak at ~25 hPa, show somewhat larger T'_B amplitudes than channel 10, consistent with larger modelled wave amplitudes at these heights (Eckermann *et al*., 2006a). All amplitudes lie well above the nominal noise floors. The consistent geolocation and orientation of the horizontal phase lines in the channel 9–11 imagery in Figure 3 indicate that the mountain wave identified at channel 9 altitudes by Eckermann *et al*. (2006a) propagates largely unaltered to the higher stratospheric altitudes imaged in channels 10 and 11.

This simple picture changes completely and abruptly on progressing still higher to channels 12–14. The channel 12 radiance perturbations at ~10 hPa in Figure 3, though again of small amplitude, nonetheless clearly show a remarkable change in horizontal phase structure. Compared to the channel 9–11 imagery, the phase lines of the channel 12 radiance perturbations have rotated anticlockwise by 30–40°. The wave pattern has also migrated south of the Scandinavian land mass to lie over Denmark and northern Germany, and the horizontal wavelength λ_h has also shortened noticeably. These same features appear with far larger radiance amplitudes in channels 13 and 14. The wave pattern also moves back towards Scandinavia slightly on ascending from channel 12 through to channel 14.

Thus, mountain waves imaged in AMSU-A's stratospheric thermal microwave radiances over southern Scandinavia on 14 January 2003 reveal strong mountain wave activity that appears to propagate through the full depth of the stratosphere. The wave observations reveal a remarkably abrupt change in overall horizontal phase structure at the channel 11–12 interface altitude of ~10–20 hPa, which persists to the highest altitude channel near the stratopause. These observed features are reproduced consistently over the ~10 hours of measurements from five separate satellite overpasses.

3.2. Cross-validation with independent Aqua measurements

An immediate question is whether these abrupt changes in imaged gravity wave structures might be some kind of observational artifact. For example, Eckermann and Wu (2006) showed that the increase in peak weighting function height with scan angle $|\beta_j|$ in Figure 1 due to the limb effect introduced small distorting curvatures to gravity wave phase lines imaged in AMSU-A radiances. To check this, here we cross-validate using independent stratospheric radiance measurements from AIRS taken during the Aqua overpass, corresponding to the third column in Figure 3. We also study waves imaged in the AAH temperature retrievals, derived from both the

DOI: 10.1002/qj

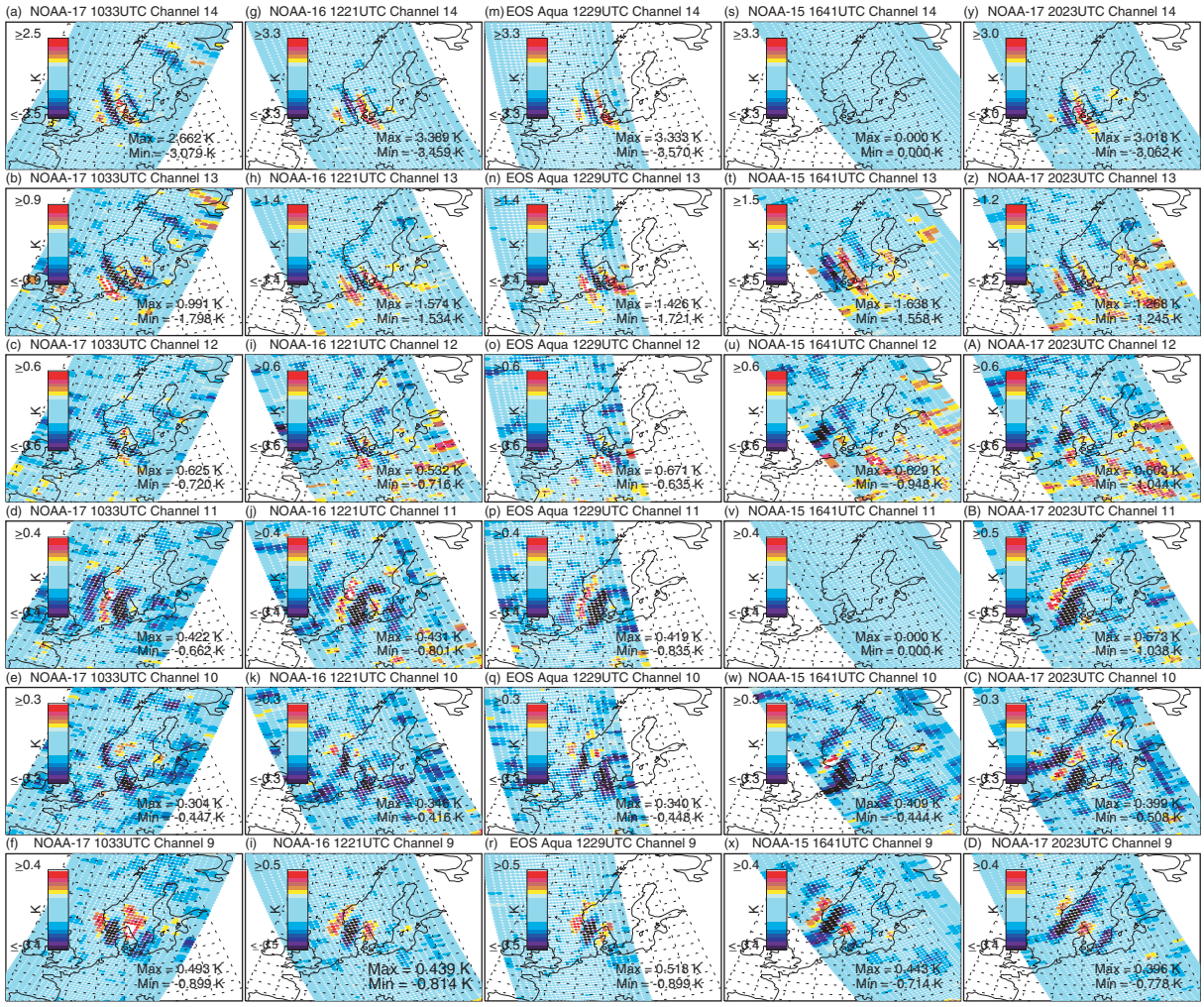

Figure 3. Time–altitude history of the mountain wave imaged over southern Scandinavia on 14 January 2003 in AMSU-A swath radiances. Columns show brightness temperature perturbations T'_B for a given AMSU-A overpass as a function of stratospheric channel altitude, ranging from lowest (channel 9, bottom row) to highest (channel 14, top row): see Figure 1. Data were smoothed using a 3 × 3 point running average to reduce noise. Successive columns show results from different satellite overpasses, arranged in chronological order from ∼1030 UTC (left column) to ∼2030 UTC (right column). Blank images in panels (s) and (v) correspond to missing data from channels 11 and 14 of the AMSU-A on NOAA-15. Values greater than (less than) each indicated colour bar range are shaded white (black). Maximum and minimum values are given at the lower right of each panel.

AMSU-A and AIRS radiances acquired during this Aqua overpass (see Section 2.2).

We isolated perturbations from AIRS radiances and AAH retrieved temperatures by fitting and removing a large-scale background using the same algorithm used for the AMSU-A radiances. For AAH temperatures, this procedure was applied at each reference pressure level p_k. Since AIRS radiances are acquired with three times greater horizontal resolution and sampling rate than AMSU-A, the numbers of AIRS points used for the along-track and cross-track smoothing and averaging calculations were all increased by a factor of 3 to maintain the same horizontal length-scales.

The resulting maps of AIRS radiance perturbations T'_B are plotted in Figure 4. Corresponding maps of AAH temperature perturbations T'_A at various pressure levels are plotted in Figure 5. In both cases, wave structures very similar to those seen in the microwave radiances in Figure 3 are evident. In particular, the abrupt change in

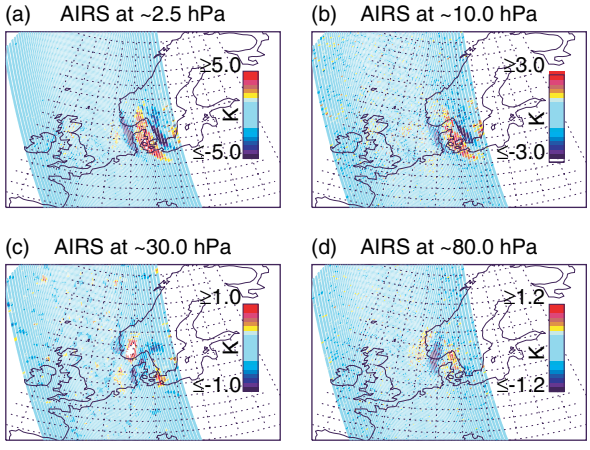

Figure 4. AIRS infrared brightness temperature perturbations T'_B during the Aqua overpass at ∼1229 UTC for channels peaking at (a) ∼2.5 hPa, (b) ∼10 hPa, (c) ∼30 hPa, and (d) ∼80 hPa. Results in (c) were smoothed using 3 × 5 point cross- and along-track averaging to accentuate wave signals.

DOI: 10.1002/qj

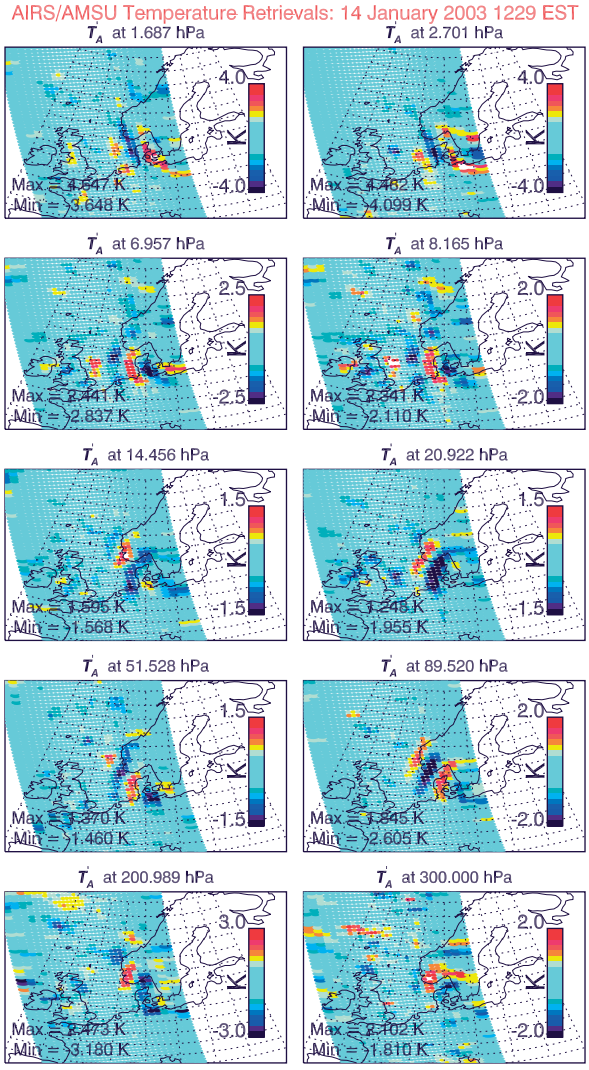

Figure 5. Perturbations in AAH retrieval temperatures T'_A from the Aqua overpass at various indicated pressure levels, after 3×3 horizontal smoothing to reduce noise. This figure is available in colour online at www.interscience.wiley.com/qj

the imaged horizontal wave phase structure at altitudes below and above ~10–20 hPa in AMSU-A radiances is also seen clearly in these fields, giving us further confidence that these are geophysically real stratospheric mountain wave signals requiring interpretation. Since the AAH temperature retrieval corrects for limb effects, these results show that this phase structure cannot be due primarily to limb distortions.

Our analysis of AAH temperatures was complicated by extended regions where the retrievals were flagged as unreliable. Most of those profiles were located within a broad open-ocean region to the west of southern Scandinavia and to the north of Scotland, where an encroaching subtropical ridge produced an elevated tropopause with high clouds (Figure 7b of McCormack *et al.*, 2004). We experimented with various algorithms that interpolated or removed these profiles, but found that retaining them in the analysis produced small T'_A values in these regions (Figure 5) and did not noticeably affect the stratospheric mountain wave signals over southern Scandinavia.

The initial T'_A maps were noisy, however, so 3×3 point horizontal averaging was applied to the fields in Figure 5 to reduce the noise and accentuate the imaged wave structures. This allows us to track the imaged wave structure in Figure 5 from the troposphere at ~300 hPa up to the stratopause. However, this horizontal averaging reduces the wave amplitudes. For example, the peak 90 hPa wave amplitude in Figure 5 is ~2.5 K, whereas the true T_{peak} inferred by Eckermann *et al.* (2006a) at this altitude is nearer 6–7 K. Unsmoothed T'_A maps (not shown) show a peak amplitude ~5 K at 90 hPa, indicating that, at this altitude at least, the temperature retrievals do a reasonable job of capturing the actual temperature amplitude of the wave. Similar conclusions were drawn by Alexander and Teitelbaum (2007) for a stratospheric mountain wave over the Antarctic Peninsula.

4. Synoptic situation

To investigate possible origins of the waves imaged in the satellite radiances and retrieved temperatures, we analyze the synoptic environment within which this mountain wave event arose.

Figure 6 plots analyzed MSLPs on 14 January 2003. The MSLPs reveal a low pressure system whose cyclonic core moved rapidly eastwards from the Norwegian Sea at 0000 UTC to cross central Scandinavia at 1200 UTC, bringing with it strong surface northwesterlies over southern Scandinavia, and weak southeasterlies over northern Scandinavia. This accounts for the strong localization of mountain wave activity to the south in Figures 3–5, since there is little surface forcing across central Scandinavia, whereas any mountain waves forced by weak southeasterlies across northern Scandinavian orography soon encounter critical levels as winds there transition to strong upper-tropospheric and stratospheric westerlies.

Accompanying this Arctic depression were strong localized jet stream winds peaking at over 70 m s^{-1} over southern Scandinavia (Figure 7(a)). Wind speeds reduced to ~30–40 m s^{-1} above this jet core and remained near this value in the stratosphere up to ~10 hPa, whereupon they increased rapidly with height to values in excess of

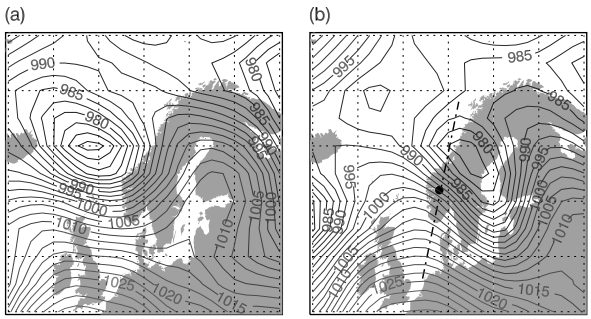

Figure 6. MSLP (hPa) from the NCEP/NCAR reanalysis at (a) 0000 UTC and (b) 1200 UTC on 14 January 2003. In (b), the broken curve and solid circle at 61°N, 8°E are used for wind profiling in Figure 7.

DOI: 10.1002/qj

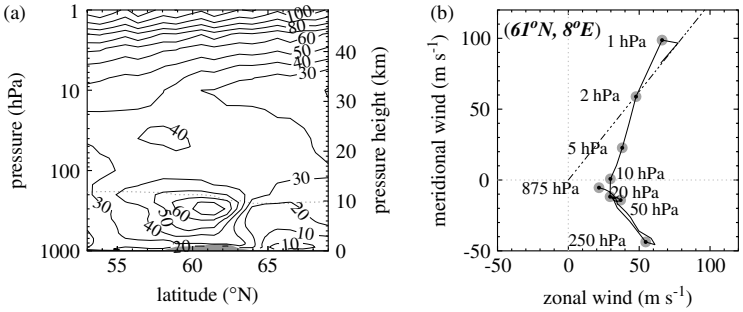

Figure 7. (a) Horizontal wind speeds (m s^{-1}) as a function of pressure and latitude along the cross-section shown as a broken curve in Figure 6(b). (b) Wind hodograph at 61 °N, 8 °E (solid circle in Figure 6(b)). Dot-dashed line is aligned at 90° to the 250 hPa wind vector. All results are from the GMAO analysis at 1200 UTC on 14 January 2003.

100 m s^{-1} (Figure 7(a)). As discussed by McCormack *et al*. (2004), the polar vortex was displaced off the pole at this time, with the edge positioned over southern Scandinavia.

Figure 7(b) shows that, from the ground to ∼20 hPa, these winds were directed to the southeast with little change in direction with altitude. Above ∼20 hPa altitude, however, winds backed (i.e. rotated anticlockwise with height) sharply, such that the winds at ∼1–2 hPa, in addition to being much stronger, were directed at close to 90° to those in the underlying jet stream core at ∼250 hPa.

While the jet stream winds over Scandinavia in Figure 7(a) show significant meridional shear, the stratospheric winds show less meridional variation. Wind speed maps over the wave region of southern Scandinavia in Figure 8 confirm that there is little zonal or meridional shear at ∼100–20 hPa, but that significant horizontal shear develops at altitudes above 20 hPa.

5. Modelling and interpretations

5.1. Effects of directional vertical shear

The southwestern portion of the Scandinavian mountains presents a large-scale quasi-elliptical obstacle to the strong surface flow in Figure 6(b). Rather than the long-wavelength plane mountain waves that are typically forced by flow across the more 2D ridge-like mountains to the north (e.g. Leutbecher and Volkert, 1996; Wirth *et al*., 1999), the orography here should launch a more 3D parabola-shaped wave pattern.

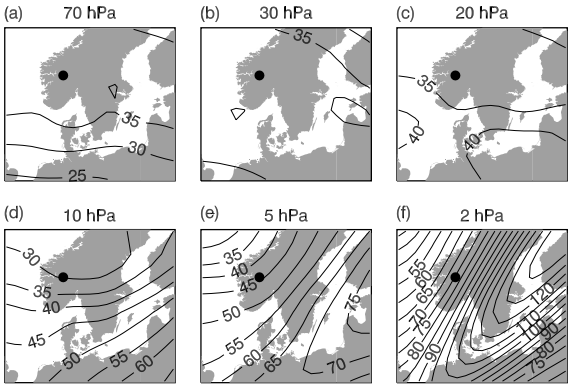

Figure 8. Mean wind speeds (m s^{-1}) from the GMAO analysis on 14 January 2003 at 1200 UTC at (a) 70 hPa, (b) 30 hPa, (c) 20 hPa, (d) 10 hPa, (e) 5 hPa, and (f) 2 hPa. Fields were smoothed zonally to remove small-scale structures. Solid circle denotes 61°N, 8°E, where profiles in Figure 7(b) used for Fourier-ray solutions are located.

When the flow direction changes with altitude, as in Figure 7(b), theory and idealized modelling for circular 3D obstacles predict that the shape, amplitude and phase-line orientation of the wave pattern vary with altitude (Shutts, 1998; Shutts and Gadian, 1999; Broutman *et al*., 2001 2002; Shutts, 2003). The strong directional shear in the wind from southeastward from 1000–20 hPa to northeastward at altitudes above ∼10 hPa coincides with the abrupt change in observed wave phase orientations in Figures 3–5.

To test whether wind turning can account for these observations, we first fitted the large-scale orography over southwestern Scandinavia to an elliptical bell-shaped function of the form

$$h(x, y) = \frac{h_{\mathrm{m}}}{\left[1 + (\widetilde{x}/a)^2 + (\widetilde{y}/b)^2\right]^{3/2}}. \qquad (4)$$

Our fit yields a peak height $h_{\mathrm{m}} = 1.5$ km, short axis width $a = 120$ km, long axis width $b = 260$ km, and orientation angle $\widetilde{\phi} = 20°$, about which the obstacle axes $(\widetilde{x}, \widetilde{y})$ are rotated from the Cartesian east–west and north–south axes (x, y). These obstacle contours are plotted in the bottom panels of Figure 9.

Next we computed Fourier-ray mountain wave solutions for representative flow over and above this obstacle. The model is forced by vertical profiles of the background wind vector $\mathbf{U}(z)$, temperature $T(z)$, Brunt–Väisälä frequency $N(z)$ and density $\rho(z)$, which we specified here using GMAO analysis fields at 61 °N, 8 °E on 14 January 2003 at 1200 UTC (solid circle in Figures 7(b) and 8).

Figure 9 profiles the resulting $T'(x, y, z)$ solutions. Figures 9(a) and 9(b) show vertical cross-sections along $y = 0$ and $x = 100$ km, respectively, as shown in Figure 9(c). From $z = 0$ to 30 km the vertical wavelengths, phase and amplitudes of these oscillations resemble those from the 3D global and mesoscale NWP model simulations of Eckermann *et al*. (2006a), for example their Figure 8.

DOI: 10.1002/qj

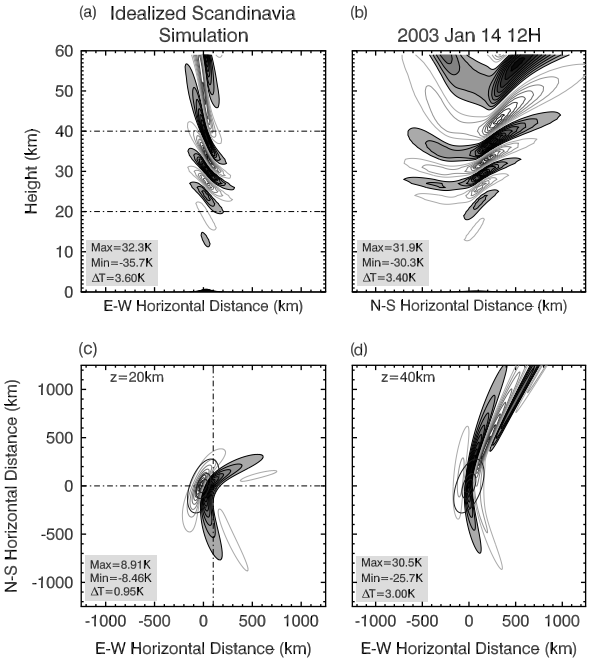

Figure 9. Steady-state Fourier-ray solutions $T'(x, y, z)$: (a) x–z cross-section at $y = 0$, (b) y–z cross-section at $x = 100$ km, and x–y cross-sections at (c) $z = 20$ km and (d) $z = 40$ km. Positive values are shaded grey. Broken lines in (c) show the x and y cross-sections in (a) and (b), while those in (a) show the z cross-sections in (c) and (d). Bold solid lines in (c) and (d) show 0.1 km, 0.5 km, and 1 km $h(x, y)$ contours for the obstacle (Equation (4)). In each panel, the contour interval and minimum and maximum values are given at the lower left.

In the hydrostatic non-rotating approximation, the vertical wavelength λ_z of a stationary mountain wave of horizontal wavenumber $\mathbf{k}_\mathrm{h} = (k, l)$ is given by

$$\lambda_z = \frac{2\pi |\mathbf{U}| |\cos(\varphi - \phi)|}{N}, \qquad (5)$$

where $\varphi - \phi$ is the difference between the wave vector and wind vector azimuths, $\varphi = \arctan(l/k)$ and $\phi = \arctan(V/U)$. At higher altitudes in Figure 9(a), λ_z values become much longer mostly, via Equation (5), in response to large increases in wind speeds $|\mathbf{U}|$ (Figure 7).

The horizontal cross-section at $z = 20$ km in Figure 9(c), corresponding roughly to the ~50 hPa peak of channel 10, reveals a 3D ship-wave pattern that is roughly symmetric about the prevailing southeastward flow direction ϕ at these altitudes and below (Figure 7(b)). The horizontal wavelength λ_h and phase are both similar to those in the channel 10 radiance patterns in Figure 3, but only above and south of the mountain; there is little or no evidence of the model's northern wing in the observations.

The $z = 40$ km fields in Figure 9(d), near the channel 13 peak at ~5 hPa, show a reduction in horizontal wavelength from the $z = 20$ km fields that is also seen in the observations. However, unlike the observations, the model fields show a weaker southern wing and larger amplitudes in a more extensive northern wing, which has rotated anticlockwise, both in location and phase line orientation, between $z = 20$ and 40 km.

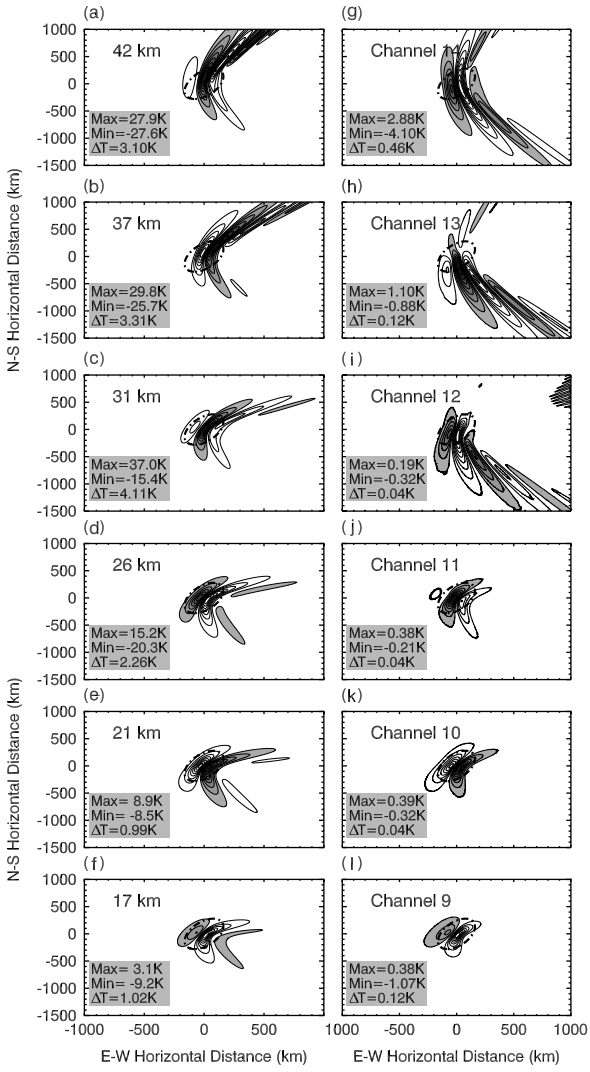

Figure 10. Left panels show steady-state Fourier-ray solutions $T'(x, y, z)$ at heights z of (a) 42 km, (b) 37 km, (c) 31 km, (d) 26 km, (e) 21 km, and (f) 17 km. Right panels show corresponding $T_\mathrm{B}^{C}(x, y)$ fields from Equation (6) for AMSU-A channels C = (g) 14, (h) 13, (i) 12, (j) 11, (k) 10, and (l) 9. In every panel, positive values are shaded grey, the $h(x, y) = 0.1$ km obstacle contour is plotted with a broken curve, and the contour interval and minimum and maximum values are given at the lower left.

The evolution of these simulated wave patterns with height is displayed in greater detail in the left column of Figure 10. The northern wing's evolution and intensification with height are consistent with idealized models of 3D mountain waves in flows that rotate anticlockwise with height. The rotating wind progessively presents directional critical levels to waves in the northern wing, such that $\varphi - \phi = \pm\pi/2$ and $\lambda_z \to 0$ from Equation (5), leaving a field of short λ_z waves at azimuths φ just ahead of the $\phi \pm \pi/2$ locus. The waves in this so-called asymptotic wake are themselves propagating ever more slowly in the vertical towards their own directional critical level located at a slightly higher altitude, and are advected long distances downstream by this flow, now directed approximately orthogonal to their $\mathbf{k}_\mathrm{h}$ vectors (Shutts, 1998; Shutts and Gadian, 1999; Broutman *et al.*, 2001, 2002), as seen in Figures 9(d),

DOI: 10.1002/qj

10(a) and 10(b). Apart from the wavelength change, the southern wing does not change as noticeably with height.

To compare more closely to the radiances in Figure 3, for a given AMSU-A channel C we computed a radiance perturbation $T_B'^C(x, y)$ by integrating that channel's 1D vertical weighting functions (1) through these model solutions, to yield

$$T_B'^C(x, y) = \int_0^{z_{top}} w_j^C(z) T'(x, y, z) dz, \qquad (6)$$

where the model top $z_{top} = 59$ km.

For simplicitly we used the weighting functions $w_j^C(z)$ from the near-zenith beam positions $j = 15–16$, plotted with solid lines on the right panels of Figure 1. A more complete and accurate forward model uses the 3D weighting functions $W_j^C(X, Y, Z)$ at all beam positions j along the satellite track (Eckermann and Wu, 2006), but then the specific overpass and scanning geometry must be used in each case (Eckermann *et al*., 2006a). The 1D approximation (Equation (6)) provides a simpler uniform upper bound on the AMSU-A brightness temperature perturbations expected from these idealized $T'(x, y, z)$ solutions. Resulting $T_B'^C(x, y)$ fields for channels $C = 9–14$ are plotted in the right panels of Figure 10.

The channel 9 $T_B'^C(x, y)$ field in Figure 10(l) has a similar orientation and geolocation to the observations in the bottom row of Figure 3, including a strong cooling phase over the mountain of ~1 K peak radiance amplitude. The channel 10 $T_B'^C(x, y)$ field in Figure 10(k) is considerably weaker in amplitude, as observed in Figure 3. The latitudinal extent of the wave pattern increases from channel 9 to channel 11, also as observed in Figure 3.

Most impressively, the wave pattern in the channel 12 $T_B'^C(x, y)$ field in Figure 10(i) shows a sudden change in location and phase line orientation compared to the channel 11 field beneath it; this is very similar in overall morphology to that observed in the AMSU-A radiances in Figure 3. Moreover, the channel 13 and 14 $T_B'^C(x, y)$ fields in Figures 10(h) and (g) show this same altered phase line structure but with progressively larger amplitudes, just as was observed in Figure 3.

Note particularly the major differences between the simulated channel 12–14 $T_B'^C(x, y)$ fields in Figure 10 and the corresponding $T'(x, y, z)$ fields near the peak of the channel weighting functions in the panels opposite. The extended large-amplitude northern wings in the $T'(x, y, z)$ above 30 km are largely eliminated from the channel 12–14 $T_B'^C(x, y)$ radiance fields, because waves in this asymptotic wake have small vertical wavelengths which make them essentially invisible to these channels (Figure 2(d)); note that the small-amplitude residual northern wing contours in Figures 10(g) and (h) have amplitudes below the nominal channel 13–14 noise floors in Table I. The channel 12–14 radiances in Figure 10 are instead dominated by wave structures in the southern wing, which extend long distances downstream of the mountain to the southeast. The horizontal wavelength, phase alignment and downstream extent of these features are all very similar to the imaged wave structure in channels 12–14 in Figure 3. The southern wing features are accentuated in the radiances because these waves have propagation azimuths φ that are roughly coaligned with the wind direction ϕ at these altitudes, which from Equation (5) yields a long vertical wavelength structure that is much more visible to these AMSU-A channels (Figure 2).

Thus, the influence of backing stratospheric flow on 3D mountain waves radiated from southern Scandianvia, coupled with the differential visibility influence of the AMSU-A weighting functions on different parts of the 3D wave field, appear to both reproduce and explain the salient features of the rotated wave phase structures observed in Figures 3–5.

One significant discrepancy remains. The simulated channel 12 and 13 $T_B'^C(x, y)$ oscillations in Figure 10 have peak amplitudes ~0.3 K and ~1.1 K, respectively, whereas the observed values in Figure 3 are about a factor of 2 larger. We investigate this issue next.

5.2. Effects of horizontal shear

The Fourier-ray simulations in Figure 9 capture only the effects of vertical shear in the background wind vector. Figure 8 reveals significant horizontal shear as well at altitudes above ~20 hPa southeastward of Scandinavia.

To model the effects on mountain waves, we performed spatial ray tracing through 3D NAVDAS/GMAO analysis fields for 14 January 2003 at 1200 UTC (see Sections 2.3 and 2.4). Our specific experiments launched rays from 61 °N, 8 °E (i.e. directly over the mountains) at a launch altitude $z_0 = 2$ km. Each ray had a stationary ground-based phase speed and constant initial horizontal wavelength $\lambda_{h_0} = 2\pi/|\mathbf{k}_{h_0}|$. Each experiment launched 13 such rays with different initial wave vector directions $\varphi_0 = \arctan(l_0/k_0)$ distributed in 10° increments between ±60°. Each ray had an initial peak horizontal velocity amplitude of 1 m s^{-1}. Horizontal wavenumbers were updated along the ray path to account for any refraction due to horizontal shears in background winds and stability (Equations (A3d) and (A3e) of Marks and Eckermann, 1995).

Figure 11 plots the resulting ray group trajectories for two separate experiments with $\lambda_{h_0} = 400$ km (top row) and 200 km (bottom row), values within the range of wavelength scales evident in Figures 3–5. The ray trajectories in each case are fairly similar, reproducing the parabola-shaped wave patterns seen in Figures 9 and 10.

The amplitudes and vertical wavelengths λ_z are depicted along the 3D ray trajectories in the right panels of Figure 11 at reference altitudes of 20, 30 and 40 km.

At $z = 20$ km, λ_z values are ~10–12 km, consistent with Fourier-ray results in Figure 9(a) (also Eckermann *et al*., 2006a). Largest amplitudes concentrate on rays located over or just south of the launch height, again consistent with Fourier-ray results in Figure 9(c) and observations in Figure 3.

DOI: 10.1002/qj

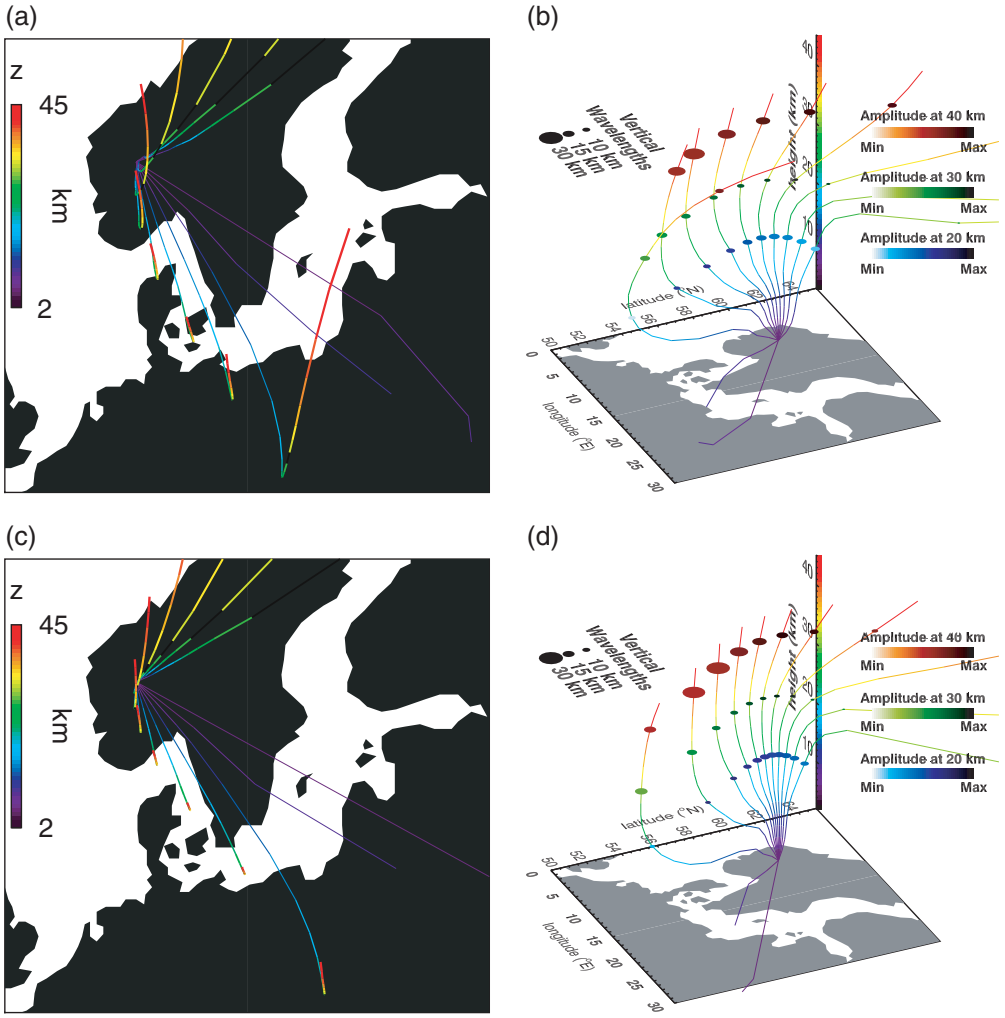

Figure 11. Ray trajectories for stationary gravity waves with $\lambda_{h_0} = 400$ km, plotted in both (a) 2D and (b) 3D. (c, d) are as (a, b), but for $\lambda_{h_0} = 200$ km. At reference altitudes of 20, 30 and 40 km, the 3D plots depict vertical wavelengths λ_z along each ray according to the size of the filled circle (see key at top left) and wave amplitude using colour scales indicated at right. See text for further details.

At 30 km altitude, corresponding roughly in altitude to channel 12, vertical wavelengths over the mountain become very short, too short for AMSU-A to resolve and consistent with an absence of resolved wave activity over the mountain in channel 12 radiances (e.g. Figures 3(i) and 3(o)). Select rays in the northeast quadrant meander obliquely downstream towards directional critical levels and attain very short vertical wavelengths, consistent with the asymptotic wake model (Shutts, 1998; Broutman *et al.*, 2002). Rays in the southeast quadrant have propagated their farthest distances from the mountain. From Figure 8(d) we see that those ray paths well to the southeast of the mountain intercept background wind speeds $|\mathbf{U}| \sim 45$ m s^{-1}, compared to values nearer 30 m s^{-1} directly over the mountain. Assuming similar wind and wave vector alignments, from Equation (5) vertical wavelengths of these far southeast rays should be around 50% longer than those near the mountain. Indeed, the longest λ_z values are seen on these far southeast rays in Figure 11, which make them the most visible to AMSU-A. Thus these ray results can explain both the southward displacement and sudden change in phase orientation of wave patterns in channel 12 compared to those in channels 9–11, since these long-λ_z rays in the southeast quadrant (the most visible to AMSU-A) have horizontal phase line orientations essentially parallel to their southeastward ground-based horizontal group trajectories in Figures 11(b) and (d) (e.g. Shutts, 1998; Broutman *et al.*, 2002).

At 40 km altitude, the ray groups in the southeastward quadrant have reversed direction to propagate back towards the mountain in response to the wind vector rotation, such that some rays have passed back over the mountain. This same behaviour is simulated with idealized linear ray models of 3D mountain waves from circular obstacles in turning shear flow (Figure 1b of Broutman *et al.*, 2002). This modelled propagation of wave activity in the southeastern quadrant back towards Scandinavia at higher altitudes is consistent with the channel 13–14 radiances in Figure 3, which show similarly aligned wave structures as in channel 12 but now located closer to the southern Scandinavian coastline.

The amplitudes of the radiance fluctuations in Figure 3 are much larger in channel 13–14 radiances than

DOI: 10.1002/qj

in channel 12. The southeast quadrant ray results in Figures 11(b) and (d) yield much longer vertical wavelengths at $z = 40$ km than at 30 km since they encounter wind speeds $|\mathbf{U}|$ of up to 50–100 m s^{-1} southeast of the mountain (Figures 8(e) and (f)), making them much more visible to AMSU-A.

These results can also explain the underestimated $T_B^{'C}(x, y)$ amplitudes from the Fourier-ray solution in Figure 10(h). The Fourier-ray model uses a single profile over the mountain where winds at 40 km are $\sim$ 40 m s^{-1} at all points in the horizontal domain. From Figure 8(e), the southeast quadrant rays in Figure 11 propagate into regions where wind speeds increase to nearer 60 m s^{-1} at 40 km, increasing vertical wavelengths in these spatial ray simulations by $\sim$50% to $\sim$25–30 km. The channel 13 visibilities in Figure 2 show that an increase in λ_z from 15–20 km to 25–30 km roughly doubles the wave visibility, exactly the increase needed to bring the $T_B^{'C}(x, y)$ amplitudes in Figure 10(h) more into line with the observed channel 13 amplitudes in Figure 3.

These spatial ray simulations also assess whether the large horizontal shears in regions southeast of the mountain in Figure 8 play any refractive role in setting the phase line orientations of waves above 20 hPa altitude. Our ray solutions do not show appreciable changes in k and l values along the southeastern rays, as evidenced by the largely linear horizontal ray path projections in Figures 11(a) and (c). The refraction of horizontal wavenumbers due to horizontal shear can be expressed approximately as (Marks and Eckermann, 1995)

$$\Delta k = -\left[k\frac{\partial U}{\partial x} + l\frac{\partial V}{\partial x}\right]\Delta t, \tag{7}$$

$$\Delta l = -\left[k\frac{\partial U}{\partial y} + l\frac{\partial V}{\partial y}\right]\Delta t. \tag{8}$$

Thus, over a given altitude interval Δz, the amount of horizontal wavenumber refraction due to horizontal shear is proportional to the ray's residence time $\Delta t = \Delta z/c_{gz}$, where c_{gz} is the vertical group velocity. The long vertical wavelengths of waves in these regions yield fast vertical group velocities and thus small residence times, which, from Equations (7) and (8), appear to limit the amount of wavenumber refraction $(\Delta k, \Delta l)$ than can accumulate along these ray paths, notwithstanding large local horizontal shears.

6. Discussion

By using data from all six stratospheric thermal channels of AMSU-A instruments on four separate satellites, as well as AIRS radiances and AAH temperature retrievals from the Aqua satellite, we have shown that the lower stratospheric mountain wave that formed over southern Scandinavia on 14 January 2003 during SOLVE II propagated through the full depth of the stratosphere. The horizontally imaged wave oscillations show a remarkable change at altitudes above $\sim$10–20 hPa; wave phase lines abruptly rotate anticlockwise and shorten in horizontal wavelength. These features persist up to the uppermost observation altitude of $\sim$2 hPa. 3D Fourier-ray and spatial ray modelling of stationary mountain wave evolution through analyzed background atmospheric conditions reproduce the salient features of these observations. There are two major influences: the observational filtering effect of the broad AMSU-A temperature weighting functions (cf. Figures 10(b) and 10(h)), and the evolution of the 3D mountain wave patterns under the influence of background stratospheric wind vectors that rotate anticlockwise and strengthen with height.

We considered and discounted other potential explanations. For example, flow over complex 3D orography forces a spectrum of waves whose different horizontal wavelengths and propagation azimuths lead, via the dispersion relation, to a spectrum of vertical group velocities, such that the shorter faster modes propagate into the middle atmosphere before the longer slower modes (e.g. Tan and Eckermann, 2000). Surface forcing over southern Scandinavia 'switches on' fairly suddenly with the arrival of the Arctic depression just after 0000 UTC (Figure 6). Thus, imaged waves at altitudes above $\sim$10–20 hPa could conceivably be mountain wave modes with faster vertical group velocities that reach these higher altitudes before the differently aligned slower wave modes imaged below $\sim$10–20 hPa altitude have had time to propagate to higher altitudes. Yet the differently aligned phase structures between channels 9–11 and 12–14 are clearly evident in Figure 3 during the 1033 UTC NOAA-17 overpass, and persist largely unchanged in all subsequent overpasses out to 2023 UTC (10 hours later). The $\lambda_h = 400$ km waves ray-traced in Section 5.2 take $\sim$10 hours to propagate from the ground to 40 km and $\sim$4–5 hours to propagate from 20 to 40 km, with times shorter for the $\lambda_h = 200$ km waves. Thus, waves at channel 9–11 altitudes during the 1033 UTC overpass should have propagated to channel 12–14 altitudes by the time of the 1641 UTC and 2023 UTC overpasses, yet imaged phase structures in Figure 3 are essentially unchanged.

So, while time variations in surface forcing and wave propagation are undoubtedly important in explaining other aspects of the mountain wave evolution on this day (e.g. differences in lower-stratospheric wave structure over time seen in Figures 3(f) and 3(D)), they cannot account for the major changes in wave structure observed across the channel 11–12 interface in Figure 3. This was confirmed by forward-modelled Fourier-ray solutions (not shown) initialized with GMAO wind and temperature profiles at 0600 UTC and 1800 UTC, which produced similar vertical variations in forward-modelled radiance structure with height to those in the 1200 UTC solutions in Figure 10.

Shutts (1998) used linear theory to study the vertical evolution of 3D hydrostatic mountain waves from a circular mountain in a simple backing wind profile of the form $\mathbf{U}(z) = (U_0, \Lambda z)$, where U_0 is the surface

DOI: 10.1002/qj

wind speed and Λ is a constant (positive) cross-shear term. Broutman *et al.* (2002) studied this same problem using a hydrostatic version of the Fourier-ray algorithm used in this study, reproducing and thus confirming Shutts' numerical predictions. The Fourier-ray simulations in Figures 9 and 10 can be viewed as a real-world application of the Shutts model, slightly generalized here to include non-hydrostatic effects and elliptical rather than circular topography, to an observed 3D mountain wave that propagated through backing horizontal winds in the stratosphere. Since the forward-modelled Fourier-ray solutions in the right panels of Figure 10 captured the unusual mountain wave structure imaged at various altitudes in Figure 3, those observations can now be interpreted as providing direct observational support for the Shutts (1998) model's predictions of how 3D mountain waves evolve in directionally sheared winds (also Shutts and Gadian, 1999; Broutman *et al.*, 2001, 2002; Shutts, 2003). While some observational evidence for this has previously been reported in the troposphere (e.g. Doyle and Jiang, 2006), Figures 3–5 appear to provide the first observational evidence of these effects operating on mountain waves in the middle atmosphere.

This 3D mountain wave transported (and ultimately deposited) large momentum fluxes into the middle atmosphere. Eckermann *et al.* (2006a) showed that its channel 9 radiance amplitude of ~0.9 K implies T_{peak} ~6–7 K. Given that these imaged channel 9 wave groups in Figure 3 are locally plane, their corresponding local vertical flux of horizontal pseudomomentum density

$$F = \frac{\rho g \lambda_z T_{\text{peak}}^2}{2\overline{T}\lambda_{\text{h}}[\mathrm{d}\overline{T}/\mathrm{d}z + \Gamma_a]}, \tag{9}$$

(Eckermann and Preusse, 1999) is ~0.3 kg m^{-1}s^{-2}. (Γ_a is the dry adiabatic lapse rate.) For 3D waves such as these, the more appropriate flux for synoptic mean-flow driving is the horizontal areal average (Shutts, 1995; Vosper and Mobbs, 1998), which will be smaller than this local value. Nonetheless, this is a large wave flux. For example, if these wave groups were uniformly and completely dissipated over a 5 km layer near 90 hPa, they would yield local mean-flow accelerations of ~50–100 m s^{-1} day^{-1}, values 1–2 orders of magnitudes larger than climatological stratospheric values (Alexander and Rosenlof, 1996).

These portions of the full 3D wave field that are resolved in the radiances do not appear to break in the stratosphere. In terms of temperature amplitudes, the convective instability threshold for wave breaking is given approximately by (e.g. Eckermann and Preusse 1999)

$$T_{\text{peak}} \geq T_{\text{break}} \approx \frac{N^2\overline{T}}{g}\frac{\lambda_z}{2\pi}. \tag{10}$$

For the imaged wave groups in channel 9 that have T_{peak} ~6–7 K, Equation (10) yields T_{break} ~15 K, implying no breaking, as the wave's continued presence at large amplitudes in channels 10 and 11 seems to attest (Figure 3). In the higher-altitude channels 12–14, the backing and intensification of **U** causes weaker amplitude waves to the south, whose $\mathbf{k}_{\text{h}}$ vectors now roughly coalign with **U**, to refract to large λ_z and become visible in these upper-level channel radiances. These increases with height in λ_z cause these waves' T_{peak} values, which from Equation (9) vary as $\sim (\rho\lambda_z)^{-1/2}$ while F remains constant, to grow with altitude more slowly, whereas T_{break} values become larger via Equation (10). Therefore the imaged wave groups at these altitudes do not appear to be breaking either. Ultimately this growth in wave amplitude with height makes it probable that the wave-breaking criterion (Equation (10)) is satisfied for these imaged wave groups somewhere in the mesosphere or lower thermosphere. Their large inferred fluxes F imply locally very large mean-flow accelerations when and where this occurs. Unfortunately there are no mesospheric satellite observations to test these inferences, since the Sounding of the Atmosphere using Broadband Emission Radiometry (SABER) instrument, which resolves gravity waves in the stratosphere and mesosphere (Preusse *et al.*, 2006), was preferentially viewing high southern latitudes at this time.

We checked our stratospheric wave breaking inferences by computing steepness fields $\eta_z(x, y, z)$ from our idealized Fourier-ray solutions in Section 5.1. These values were all less than unity (i.e. statically stable) at $z = 20$, 30 and 40 km in these southern wing regions. However, wave fields over the mountain and in the northern wing, which were simulated in Figures 9 and 10 but not resolved in the satellite radiances due to their shorter λ_z values, yielded unstable steepness values above ~30 km. This is entirely consistent with Equation (10), since the small λ_z values that make these wave groups invisible in the radiances also yield much smaller wave-breaking amplitudes T_{break}. As **U** backs in the upper stratosphere, λ_z and T_{break} values in the northern wing decrease with height, becoming very small near directional critical levels in the asymptotic wake as $\mathbf{k}_{\text{h}}.\mathbf{U} \rightarrow 0$ (Shutts, 1998). As their wave amplitudes continue to grow with height, Equation (10) implies progressive breaking of the waves in these regions throughout the upper stratosphere, along the lines predicted by idealized models of 3D mountain waves in backing flows (e.g. Broad, 1999; Shutts and Gadian, 1999; Broutman *et al.*, 2001; Shutts, 2003). The resulting directional deposition of wave momentum flux into this rotating mean flow may have potentially interesting effects on the mean state that are not found in standard 2D wave mean-flow interaction models (e.g. Martin and Lott, 2007).

These findings are therefore relevant to how subgrid-scale orographic gravity wave drag (OGWD) is parametrized in global middle atmosphere climate models, which typically run at resolutions that would not resolve this wave event. Most OGWD parametrizations specify a single plane 2D wave, with $\mathbf{k}_{\text{h}}$ directed either against the surface flow (Palmer *et al.*, 1986; McFarlane, 1987; Gregory *et al.*, 1998) or orthogonal to the dominant topographic alignment (Bacmeister, 1993; Lott and

DOI: 10.1002/qj

Miller, 1997). The early single-wave OGWD schemes produced excessively large and abrupt stratospheric drag in models (Klinker and Sardeshmukh, 1992; Hogan and Brody, 1993; Milton and Wilson, 1996). To mitigate this, some models eliminated parametrized OGWD above the tropopause (e.g. Hogan and Brody, 1993; Norton and Thuburn, 1999). Others assigned a smaller fraction of the total pressure drag across the subgrid-scale orography to vertically propagating OGWs and a greater fraction to near-surface drag from flow blocking, lee vortices and low-level wave breaking (e.g. Webster *et al*., 2003).

Single-wave schemes cannot capture the gradual erosion of momentum flux with altitude and the directional drag that we have inferred for this observed 3D mountain wave due to the backing shear flow in the stratosphere. The spatial ray results in Figure 11 indicate that an OGWD scheme propagating a number of waves with differently aligned $\mathbf{k}_h$ vectors into the atmosphere (e.g. Shutts, 1995; Eckermann *et al*., 2006b) is needed. The more gradual and realistic directional deposition of flux with altitude that results might also ameliorate some of the excessive stratospheric OGWD that single-wave schemes have produced in models. A step in this direction was taken by Scinocca and McFarlane (2000), whose OGWD scheme launches two OGWs whose $\mathbf{k}_h$ orientations and momentum fluxes are determined by the parametrized 3D obstacle properties and surface flow conditions. They reported that their two-wave scheme transported ∼30–50% more OGW momentum flux through the middle atmosphere than the single-wave scheme of McFarlane (1987).

Whether the computational overhead of a multiwave OGWD scheme is justified by noticeably improved climate or forecast skill is as yet unclear. In particular, further observations and modelling are needed to assess the broader relevance of directionally filtered and dissipated 3D mountain waves to the momentum budget of the middle atmosphere. The high-resolution global data provided by AMSU-A, AIRS and other satellite instruments (e.g. Wu *et al*., 2006) should allow other case-studies to be identified and analyzed with these issues in mind.

7. Conclusions

Data from all six AMSU-A stratospheric thermal channels have shown that the PSC-producing lower-stratospheric mountain wave, observed during SOLVE II and analyzed by Eckermann *et al*. (2006a), propagates through the entire stratosphere. The radiance perturbation maps revealed major differences in the horizontally imaged wave phase structure below and above ∼10–20 hPa. Similar features were also seen in AIRS radiances and AAH temperature retrievals from the Aqua overpass, confirming their geophysical origin.

This interface altitude corresponded to the onset of anticlockwise rotation and intensification of background stratospheric winds over the mountain. Fourier-ray simulations, using an 3D elliptical obstacle to represent southern Scandinavian orography and realistic background wind and temperature profiles, yielded a 3D mountain wave that propagated to the stratopause. While this was in qualititative agreement with the observations, the modelled 2D horizontal temperature oscillations differed noticeably from the radiance imagery, particularly in the high-altitude channels. On converting model fields to channel radiances using a simple forward model, the model-generated radiance oscillations agreed much better with the observations in each channel. In particular, the abrupt change in structure of imaged radiance oscillations between channels 11 and 12 was convincingly reproduced. Spatial ray simulations showed that horizontal shear at altitudes above ∼20 hPa increased vertical wavelengths to the south, further accentuating these structures in the AMSU-A imagery.

In addition to the important visibility effects of the channel weighting functions acting on different portions of the 3D wave pattern, the modelled response of waves to anticlockwise rotation and intensification of stratospheric winds was also key to reproducing the observations. The Fourier-ray model solutions generated here can be viewed as generalizing the idealized linear 3D wave solutions of Shutts (1998) to more complex background profiles and elliptical rather than circular topography. Thus, the close agreement between the observed radiance oscillations and the forward-modelled Fourier-ray solutions constitutes experimental support for the Shutts model's predictions of the vertical evolution of 3D mountain waves in directionally sheared flow. For example, the ray solutions revealed an additional northern wing of wave activity that attains breaking amplitudes in the stratosphere, due to shorter vertical wavelengths that make the wave activity here invisible to AMSU-A. The waves here evolve with height and break according to Shutts' 'asymptotic wake' model (Shutts, 1998; Broad, 1999; Shutts and Gadian, 1999; Broutman *et al*., 2001).

The waves imaged by AMSU-A in the southern wing had large vertical fluxes of horizontal pseudomomentum density (F ∼0.3 kg m^{-1}s^{-2}). Modelling and theoretical diagnostics both indicated that these wave groups did not break in the stratosphere, but probably broke in the mesosphere or lower thermosphere.

The observations and modelling together imply a progressive directional deposition of this 3D wave's momentum flux throughout the middle atmosphere, which contrasts with the simpler 2D plane-wave methods most often currently used to parametrize unresolved OGWD in climate and NWP models.

Acknowledgements

SDE thanks his NRL Monterey colleagues Ben Ruston, for his help with the CRTM, and Tim Hogan, for generating the NAVDAS reanalysis fields. He also thanks Joan Alexander and Lars Hoffmann for helpful discussions about the AAH temperature retrievals. This work was partially supported by NASA's Geospace Sciences SR&T program and Earth Sciences programs NNH04ZYS004N (Measurements, Modeling, and Analyses in Support of

DOI: 10.1002/qj

AURA and other NASA Satellite Observations of the Earth's Atmosphere) and NNH06ZDA001N-EOS (Earth System Science Research using Data and Products from the Terra, Aqua, and ACRIMSAT Satellites). DB was funded by the National Science Foundation, grant ATM-044888. DLW's work was conducted at the Jet Propulsion Laboratory, California Institute of Technology, under a contract with NASA. We thank three anonymous reviewers for a number of constructive comments that improved the paper.

References

Alexander MJ, Rosenlof KH. 1996. Nonstationary gravity wave forcing of the stratospheric zonal mean wind. *J. Geophys. Res.* **101**: 23465–23474.

Alexander MJ, Barnet C. 2007. Using satellite observations to constrain parameterizations of gravity wave effects for global models. *J. Atmos. Sci.* **64**: 1652–1665.

Alexander MJ, Teitelbaum H. 2007. Observation and analysis of a large amplitude mountain wave event over the Antarctic peninsula. *J. Geophys. Res.* **112**: D21103, DOI:10.1029/2006JD008368.

Aumann HH, Chahine MT, Gautier C, Goldberg MD, Kalnay E, McMillin LM, Revercomb H, Rosenkranz PW, Smith WL, Staelin DH, Strow LL, Susskind J. 2003. AIRS/AMSU/HSB on the Aqua mission: design, science objectives, data products, and processing systems. *IEEE Trans. Geosci. Remote Sensing* **41**: 253–264.

Bacmeister JT. 1993. Mountain-wave drag in the stratosphere and mesosphere inferred from observed winds and a simple mountain-wave parameterization scheme. *J. Atmos. Sci.* **50**: 377–399.

Bloom S, da Silva A, Dee D, Bosilovich M, Chern J-D, Pawson S, Schubert S, Sienkiewicz M, Stajner I, Tan W-W, Wu M-L. 2005. Documentation and validation of the Goddard Earth Observing System (GEOS) data assimilation system – version 4. NASA Technical Report Series on Global Modeling and Data Assimilation, Suarez MJ. (ed.) **26**: Tech. Mem. NASA/TM-2005-104 606, available at http://ntrs.nasa.gov.

Blum U, Baumgarten G, Schöch A, Kirkwood S, Naujokat B, Fricke KH. 2006. The atmospheric background situation in northern Scandinavia during January/February 2003 in the context of the MaCWAVE campaign. *Ann. Geophys.* **24**: 1189–1197.

Broad A. 1999. Do orographic gravity waves break in flows with uniform wind direction turning with height? *Q. J. R. Meteorol. Soc.* **125**: 1695–1714.

Broutman D, Rottman JW, Eckermann SD. 2001. A hybrid method for analyzing wave propagation from a localized source, with application to mountain waves. *Q. J. R. Meteorol. Soc.* **127**: 129–146.

Broutman D, Rottman JW, Eckermann SD. 2002. Maslov's method for stationary hydrostatic mountain waves. *Q. J. R. Meteorol. Soc.* **128**: 1159–1172.

Broutman D, Rottman JW, Eckermann SD. 2003. A simplified Fourier method for nonhydrostatic mountain waves. *J. Atmos. Sci.* **60**: 2686–2696.

Carslaw KS, Wirth M, Tsias A, Luo BP, Dörnbrack A, Leutbecher M, Volkert H, Renger W, Bacmeister JT, Reimer E, Peter T. 1998. Increased stratospheric ozone depletion due to mountain-induced atmospheric waves. *Nature* **391**: 675–678.

Carslaw KS, Peter T, Bacmeister JT, Eckermann SD. 1999. Widespread solid particle formation by mountain waves in the Arctic stratosphere. *J. Geophys. Res.* **104**: 1827–1836.

Chahine MT, Pagano TS, Aumann HH, Atlas R, Barnet C, Blaisdell J, Chen L, Divakarla M, Fetzer EJ, Goldberg M, Gautier C, Granger S, Hannon S, Irion FW, Kakar R, Kalnay E, Lambrigtsen BH, Lee S-Y, Le Marshall J, McMillan WW, McMillin L, Olsen ET, Revercomb H, Rosenkranz P, Smith WL, Staelin D, Strow LL, Susskind J, Tobin D, Wolf W, Zhou L. 2006. AIRS: Improving weather forecasting and providing new data on greenhouse gases. *Bull. Am. Meteorol. Soc.* **87**: 911–926.

Davies LA, Brown AR. 2001. Assessment of which scales of orography can be credibly resolved in a numerical model. *Q. J. R. Meteorol. Soc.* **127**: 1225–1237.

Deshler T, Peter T, Müller R, Crutzen P. 1994. The lifetime of leewave-induced particles in the Arctic stratosphere: 1. Ballonborne observations. *Geophys. Res. Lett.* **21**: 1327–1330.

Dörnbrack A, Leutbecher M, Volkert H, Wirth M. 1998. Mesoscale forecasts of stratospheric mountain waves. *Meteorol. Appl.* **5**: 117–126.

Dörnbrack A, Leutbecher M, Reichardt J, Behrendt A, Müller KP, Baumgarten G. 2001. Relevance of mountain wave cooling for the formation of polar stratospheric clouds over Scandinavia: Mesoscale dynamics and observations for January 1997. *J. Geophys. Res.* **106**: 1569–1582.

Doyle JD, Jiang Q. 2006. Observations and numerical simulations of mountain waves in the presence of directional wind shear. *Q. J. R. Meteorol. Soc.* **132**: 1877–1905.

Eckermann SD, Marks CJ. 1997. GROGRAT: A new model of the global propagation and dissipation of atmospheric gravity waves. *Adv. Space Res.* **20**(6): 1253–1256.

Eckermann SD, Preusse P. 1999. Global measurements of stratospheric mountain waves from space. *Science* **286**: 1534–1537.

Eckermann SD, Wu DL. 2006. Imaging gravity waves in lower stratospheric AMSU-A radiances, Part 1: Simple forward model. *Atmos. Chem. Phys.* **6**: 3325–3341.

Eckermann SD, Gibson-Wilde DE, Bacmeister JT. 1998. Gravity wave perturbations of minor constituents: A parcel advection methodology. *J. Atmos. Sci.* **55**: 3521–3539.

Eckermann SD, Wu DL, Doyle JD, Burris JF, McGee TJ, Hostetler CA, Coy L, Lawrence BN, Stephens A, McCormack JP, Hogan TF. 2006a. Imaging gravity waves in lower stratospheric AMSU-A radiances, Part 2: Validation case study. *Atmos. Chem. Phys.* **6**: 3343–3362.

Eckermann SD, Dörnbrack A, Vosper SB, Flentje H, Mahoney MJ, Bui TP, Carslaw KS. 2006b. Mountain wave-induced polar stratospheric cloud forecasts for aircraft science flights during SOLVE/THESEO 2000. *Weather and Forecasting* **21**: 42–68.

Fritts DC, Rastogi PK. 1985. Convective and dynamical instabilities due to gravity wave motions in the lower and middle atmosphere: Theory and observations. *Radio Sci.* **20**: 1247–1277.

Fueglistaler S, Buss S, Luo BP, Wernli H, Flentje H, Hostetler CA, Poole LR, Carslaw KS, Peter T. 2003. Detailed modeling of mountain wave PSCs. *Atmos. Chem. Phys.* **3**: 697–712.

Garcia RR, Boville BA. 1994. 'Downward control' of the mean meridional circulation and temperature distribution of the polar winter stratosphere. *J. Atmos. Sci.* **51**: 2238–2245.

Godin S, Mégie G, David C, Haner D, Flesia C, Emery Y. 1994. Airborne lidar observations of mountain-wave-induced polar stratospheric clouds during EASOE. *Geophys. Res. Lett.* **21**: 1335–1338.

Goldberg MD, Crosby DS, Zhou L. 2001. The limb adjustment of AMSU-A observations: Methodology and validation. *J. Appl. Meteorol.* **40**: 70–83.

Goldberg RA, Fritts DC, Schmidlin FJ, Williams BP, Croskey CL, Mitchell JD, Friedrich M, Russell III JM, Blum U, Fricke KH. 2006. The MaCWAVE program to study gravity wave influences on the polar mesosphere. *Annales Geophysicae* **24**: 1159–1173.

Gregory DG, Shutts GJ, Mitchell JR. 1998. A new gravity wave drag scheme incorporating anisotropic orography and low-level wave breaking: Impact upon the climate of the UK Meteorological Office unified model. *Q. J. R. Meteorol. Soc.* **124**: 463–494.

Hertzog A, Vial F, Dörnbrack A, Eckermann SD, Knudsen BM, Pommereau J-P. 2002. In-situ observations of gravity waves and comparisons with numerical simulations during the SOLVE/THESEO 2000 campaign. *J. Geophys. Res.* **107**(D20): 8292, DOI: 10.1029/2001JD001025.

Hogan TF, Brody LR. 1993. Sensitivity studies of the Navy's global forecast model parameterizations and evaluation of improvements to NOGAPS. *Mon. Weather Rev.* **121**: 2373–2395.

Kleespies TJ, van Delst P, McMillin LM, Derber J. 2004. Atmospheric transmittance of an absorbing gas. 6: OPTRAN status report and introduction to the NESDIS/NCEP community radiative transfer model. *Appl. Opt.* **43**: 3103–3109.

Klinker E, Sardeshmukh PD. 1992. The diagnosis of mechanical dissipation in the atmosphere from large-scale balance requirements. *J. Atmos. Sci.* **49**: 608–627.

Kühl S, Dörnbrack A, Wilms-Grabe W, Sinnhuber B-M, Platt U, Wagner T. 2004. Observational evidence of rapid chlorine activation by mountain waves above northern Scandinavia. *J. Geophys. Res.* **109**: D22309, DOI:10.1029/2004JD004797.

Lambrigtsen BH. 2003. Calibration of the AIRS microwave instruments. *IEEE Trans. Geosci. Remote Sensing* **41**: 369–378.

Lambrigtsen BH, Calheiros RV. 2003. The Humidity Sounder for Brazil – an international partnership. *IEEE Trans. Geosci. Remote Sensing* **41**: 352–361.

Leutbecher M, Volkert H. 1996. Stratospheric temperature anomalies and mountain waves: A three-dimensional simulation using a multi-scale weather prediction model. *Geophys. Res. Lett.* **23**: 3329–3332.
Lott F, Miller MJ. 1997. A new subgrid-scale orographic drag parametrization: Its formulation and testing. *Q. J. R. Meteorol. Soc.* **123**: 101–127.
Lowe D, MacKenzie AR, Schlager H, Voigt C, Dörnbrack A, Mahoney MJ, Cairo F. 2006. Liquid particle composition and heterogeneous reactions in a mountain wave polar stratospheric cloud. *Atmos. Chem. Phys.* **6**: 3611–3623.
Mann GW, Carslaw KS, Chipperfield MP, Davies S, Eckermann SD. 2005. Large nitric acid trihydrate particles and denitrification caused by mountain waves in the Arctic stratosphere. *J. Geophys. Res.* **110**: D08202, DOI: 10.1029/2004JD005271.
Marks CJ, Eckermann SD. 1995. A three-dimensional nonhydrostatic ray-tracing model for gravity waves: Formulation and preliminary results for the middle atmosphere. *J. Atmos. Sci.* **52**: 1959–1984.
Martin A, Lott F. 2007. Synoptic responses to mountain gravity waves encountering directional critical levels. *J. Atmos. Sci.* **64**: 828–848.
McCormack JP, Eckermann SD, Coy L, Allen DR, Kim Y-J, Hogan T, Lawrence BN, Stephens A, Browell EV, Burris J, McGee T, Trepte CR. 2004. NOGAPS-ALPHA model simulations of stratospheric ozone during the SOLVE2 campaign. *Atmos. Chem. Phys.* **4**: 2401–2423.
McFarlane NA. 1987. The effect of orographically excited gravity wave drag on the general circulation of the lower stratosphere and troposphere. *J. Atmos. Sci.* **44**: 1775–1800.
McLandress C. 1998. On the importance of gravity waves in the middle atmosphere and their parameterization in general circulation models. *J. Atmos. Solar-Terr. Phys.* **60**: 1357–1383.
Milton SF, Wilson CA. 1996. The impact of parameterized subgrid-scale orographic forcing on systematic errors in a global NWP model. *Mon. Weather Rev.* **124**: 2023–2045.
Mo T. 1999. AMSU-A antenna pattern corrections. *IEEE Trans. Geosci. Remote Sensing* **37**: 103–112.
Newman PA, Harris NRP, Adriani A, Amanatidis GT, Anderson JG, Braathen GO, Brune WH, Carslaw KS, Craig MS, DeCola PL, Guirlet M, Hipskind RS, Kurylo MJ, Küllmann H, Larsen N, Mégie GJ, Pommereau J-P, Poole LR, Schoeberl MR, Stroh F, Toon OB, Trepte CR, Van Roozendael M. 2002. An overview of the SOLVE/THESEO 2000 campaign. *J. Geophys. Res.* **107**: 8259, DOI: 10.1029/2001JD001303.
Norton WA, Thuburn J. 1999. Sensitivity of mesospheric mean flow, planetary waves, and tides to strength of gravity wave drag. *J. Geophys. Res.* **104**: 30897–30911.
Palmer TN, Shutts GJ, Swinbank R. 1986. Alleviation of a systematic westerly bias in general circulation and numerical weather prediction models through an orographic gravity wave drag parameterization. *Q. J. R. Meteorol. Soc.* **112**: 1001–1039.
Pierce RB, Al-Saadi J, Fairlie TD, Natarajan M, Harvey VL, Grose WL, Russell JM, Bevilacqua R, Eckermann SD, Fahey D, Popp P, Richard E, Stimpfle R, Toon GC, Webster CR, Elkins J. 2003. Large-scale chemical evolution of the Arctic vortex during the 1999/2000 winter: HALOE/POAM III Lagrangian photochemical modeling for the SAGE IIIO-zone Loss and Validation Experiment (SOLVE) campaign. *J. Geophys. Res.* **108**(D5): 8317, DOI: 10.1029/2001JD001063.
Preusse P, Dörnbrack A, Eckermann SD, Riese M, Schaeler B, Bacmeister JT, Broutman D, Grossmann KU. 2002. Space-based measurements of stratospheric mountain waves by CRISTA. 1: Sensitivity, analysis method, and a case study. *J. Geophys. Res.* **107**(D23): 8178, DOI: 10.1029/2001JD000699.
Preusse P, Ern M, Eckermann SD, Warner CD, Picard RH, Knieling P, Krebsbach M, Russell III JM, Mlynczak MG, Mertens CJ, Riese M. 2006. Tropopause to mesopause gravity waves in August: Measurement and modeling. *J. Atmos. Solar-Terr. Phys.* **68**: 1730–1751.
Pyle JA, Harris NRP, Farman JC, Arnold F, Braathen G, Cox RA, Faucon P, Jones RL, Megie G, O'Neill A, Platt U, Pommereau J-P, Schmidt U, Stordal F. 1994. An overview of the EASOE campaign. *Geophys. Res. Lett.* **21**: 1191–1194.
Rosenkranz PW. 2003. Rapid radiative transfer model for AMSU/HSB channels. *IEEE Trans. Geosci. Remote Sensing* **41**: 362–368.
Scinocca JF, McFarlane NA. 2000. The parameterization of drag induced by stratified flow over anisotropic orography. *Q. J. R. Meteorol. Soc.* **126**: 2353–2393.
Shutts GJ. 1995. Gravity-wave drag parametrization over complex terrain: The effect of critical-level absorption in directional wind-shear. *Q. J. R. Meteorol. Soc.* **121**: 1005–1021.
Shutts GJ. 1998. Stationary gravity-wave structure in flows with directional wind shear. *Q. J. R. Meteorol. Soc.* **124**: 1421–1442.
Shutts GJ. 2003. Inertia-gravity wave and neutral Eady wave trains forced by directionally sheared flow over isolated hills. *J. Atmos. Sci.* **60**: 593–606.
Shutts GJ, Gadian A. 1999. Numerical simulations of orographic gravity waves in flows which back with height. *Q. J. R. Meteorol. Soc.* **125**: 2743–2765.
Siskind DE, Eckermann SD, Coy L, McCormack JP, Randall CE. 2007. On recent interannual variability of the Arctic winter mesosphere: Implications for tracer descent. *Geophys. Res. Lett.* **34**: L09806, DOI: 10.1029/2007GL029293.
Skamarock WC. 2004. Evaluating mesoscale NWP models using kinetic energy spectra. *Mon. Weather Rev.* **132**: 3019–3032.
Stajner I, Benson C, Liu H-C, Pawson S, Brubaker N, Chang L-P, Riishojgaard LP, Todling R. 2007. Ice polar stratospheric clouds detected from assimilation of Atmospheric Infrared Sounder data. *Geophys. Res. Lett.* **34**: L16802, DOI: 10.1029/2007GL029415.
Stefanutti L, MacKenzie AR, Balestri S, Khattatov V, Fiocco G, Kyro E, Peter T. 1999. Airborne Polar Experiment/Polar Ozone, Lee-waves, Chemistry and Transport (APE/POLECAT): Rationale, road map and summary of measurements. *J. Geophys. Res.* **104**: 23941–23959.
Susskind J, Barnet CD, Blaisdell JM. 2003. Retrieval of atmospheric and surface parameters from AIRS/AMSU/HSB data in the presence of clouds. *IEEE Trans. Geosci. Remote Sensing* **41**: 390–409.
Susskind J, Barnet C, Blaisdell J, Iredell L, Keita F, Kouvaris L, Molnar G, Chahine M. 2006. Accuracy of geophysical parameters derived from Atmospheric Infrared Sounder/Advanced Microwave Sounding Unit as a function of fractional cloud cover. *J. Geophys. Res.* **111**: D09S17, DOI: 10.1029/2005JD006272.
Tan KA, Eckermann SD. 2000. Numerical model simulations of mountain waves in the middle atmosphere over the southern Andes. Pp 311–318 in *Atmospheric Science Across the Stratopause*, AGU Monograph Series **123**.
Turco R, Plumb A, Condon E. 1990. The Airborne Arctic Stratospheric Experiment: Prologue. *Geophys. Res. Lett.* **17**: 313–316.
Volkert H, Intes D. 1992. Orographically forced stratospheric waves over northern Scandinavia. *Geophys. Res. Lett.* **19**: 1205–1208.
Vosper SB, Mobbs SD. 1998. Momentum fluxes due to three-dimensional gravity-waves: Implications for measurements and numerical modelling. *Q. J. R. Meteorol. Soc.* **124**: 2755–2769.
Webster S, Brown AR, Cameron DR, Jones CP. 2003. Improvements to the representation of orography in the Met Office Unified Model. *Q. J. R. Meteorol. Soc.* **129**: 1989–2010.
Wirth M, Tsias A, Dörnbrack A, Weiss V, Carslaw KS, Leutbecher M, Renger W, Volkert H, Peter T. 1999. Model-guided Lagrangian observation and simulation of mountain polar stratospheric clouds. *J. Geophys. Res.* **104**(D19): 23971–23982.
Wu DL. 2004. Mesoscale gravity wave variances from AMSU-A radiances. *Geophys. Res. Lett.* **31**: L112114, DOI: 10.1029/2004GL019562.
Wu DL, Eckermann SD. 2007. Global gravity wave variances from Aura MLS: Characteristics and interpretation. *J. Atmos. Sci.* (in press).
Wu DL, Preusse P, Eckermann SD, Jiang JH, de la Torre Juarez M, Coy L, Wang DY. 2006. Remote sounding of atmospheric gravity waves with satellite limb and nadir techniques. *Adv. Space Res.* **37**: 2269–2277.
Zhu X. 1993. Radiative damping revisited: Parameterization of damping rate in the middle atmosphere. *J. Atmos. Sci.* **50**: 3008–3021.